

## WIND INHOMOGENEITIES IN WOLF-RAYET STARS. II. INVESTIGATION OF EMISSION-LINE PROFILE VARIATIONS

SÉBASTIEN LÉPINE<sup>1</sup> AND ANTHONY F. J. MOFFAT<sup>2</sup>

Département de Physique, Université de Montréal, and Observatoire du Mont-Mégantic, C.P. 6128, Succ. Centre-Ville, Montréal, QC, CANADA H3C 3J7; lepine@astro.umontreal.ca, moffat@astro.umontreal.ca

*Received 1997 September 9; accepted 1998 August 4*

### ABSTRACT

We present high-resolution spectroscopic monitoring of the line-profile variations (LPVs) in the He II  $\lambda 5411$  emission line of four Wolf-Rayet (WR) stars of the WN sequence (HD 96548, HD 191765, HD 192163, and HD 193077) and in the C III  $\lambda 5696$  emission line of five WR stars of the WC sequence (HD 164270, HD 165763, HD 192103, HD 192641, and HD 193793). The LPVs are shown to present systematic patterns: they all consist of a number of relatively narrow emission subpeaks that tend to move from the line centers toward the line edges. We introduce a phenomenological model that depicts WR winds as being made up of a large number of randomly distributed, radially propagating, discrete wind emission elements (DWEs). This working model is used to simulate LPV patterns in emission lines from a clumped wind. General properties of the LPV patterns are analyzed with the help of novel numerical tools (based on multiscale, wavelet analysis), and simulations are compared to the data. We investigate the effects on the LPVs of local velocity gradients, optical depths, various numbers of discrete wind elements, and a statistical distribution in the line flux from individual elements. We also investigate how the LPV patterns are affected by the velocity structure of the wind and by the extension of the line-emission region (LER). Eight of the stars in our sample are shown to possess strong similarities in their LPV patterns, which can all be explained in terms of our simple model of local wind inhomogeneities. We find, however, that a very large number ( $\geq 10^4$ ) of DWEs must be used to account for the LPV. Large velocity dispersions must occur within DWEs, which give rise to the  $\overline{\sigma}_\xi \sim 100 \text{ km s}^{-1}$  line-of-sight velocity dispersions. We find evidence for anisotropy in the velocity dispersion within DWEs with  $\sigma_{v_r} \sim 4\sigma_{v_\theta}$ , where  $\sigma_{v_r}$  and  $\sigma_{v_\theta}$  are the velocity dispersions in the radial and azimuthal directions, respectively. We find marginal evidence for optical depth effects within inhomogeneous features, with the escape probability being slightly smaller in the radial direction. The kinematics of the variable features reveals lower than expected radial accelerations, with  $20 < \beta R_*(R_\odot) < 80$ , where  $\beta$  and  $R_*$  are parameters of the commonly used velocity law  $v(r) = v_\infty(1 - R_*r^{-1})^\beta$ , with  $v_\infty$  the terminal wind velocity. The mean duration of subpeak events, interpreted as the crossing time of DWEs through the LER, is found to be consistent with a relatively thin LER. As a consequence, the large emission-line broadening cannot be accounted for by the systematic radial velocity gradient from the accelerating wind. Rather, emission-line broadening must be dominated by the large “turbulent” velocity dispersion  $\sigma_{v_r}$  suggested by the LPV patterns. The remaining WR star in our sample (HD 191765) is shown to present significant differences from the others in its LPV pattern. In particular, the associated mean velocity dispersion is found to be especially large ( $\overline{\sigma}_\xi \sim 350 \text{ km s}^{-1}$ , compared to  $\overline{\sigma}_\xi \sim 100 \text{ km s}^{-1}$  in other stars). Accordingly, the LPV patterns in HD 191765 cannot be satisfactorily accounted for with our model, requiring a different origin.

*Subject headings:* instabilities — line: profiles — stars: mass loss — stars: Wolf-Rayet — turbulence

### 1. INTRODUCTION

The spectra of Wolf-Rayet (WR) stars are dominated by broad emission lines of Helium, with lines of nitrogen in stars of the WN sequence, or carbon and oxygen in stars of the WC/WO sequence. These lines are sometimes accompanied by blueshifted P Cygni absorption features. The generally accepted interpretation is that the lines are formed in extended regions of a fast ( $\sim 10^3 \text{ km s}^{-1}$ ), dense ( $\sim 10^{-5} M_\odot \text{ yr}^{-1}$ ) stellar wind (see, e.g., Willis 1991). The spectral analysis of WR stars is made difficult by the fact that the usual assumptions of local thermodynamic equilibrium and plane-parallel atmospheres do not apply. Moreover, WR winds are believed to be stratified in ionization (see, e.g., Schulte-Ladbeck, Eenens, & Davis 1995), which means

that emission lines from different atomic transitions are formed at different depths in the wind.

Current models of WR atmospheres rely on a set of simplifying assumptions within the framework of the so-called “standard model” (see, e.g., Hillier 1995; Hamann 1995, and references therein), which describes the formation of emission lines in a dense wind photoionized by a hot core. In the standard model, it is assumed that the wind is spherically symmetric, homogeneous, and stationary. Radiative and statistical equilibrium are adopted, and a monotonic wind velocity law is fixed a priori. These assumptions have been used to perform spectral analyses of WR spectra and to predict effective temperatures and luminosities. However, several systematic deficiencies have been observed (see, e.g., Howarth & Schmutz 1992; Hamann, Wessolowski, & Koesterke 1994; Hillier 1996; Schmutz 1997), suggesting that at least some assumptions in the standard model are invalid.

The picture of a smooth, homogeneous wind in WR stars

<sup>1</sup> Present address: Space Telescope Science Institute, 3700 San Martin Drive, Baltimore, MD 21218; lepine@stsci.edu.

<sup>2</sup> Killam Research Fellow of the Canada Council for the Arts.

is being challenged by several lines of observational evidence (see Moffat 1996). Since it is believed that inhomogeneous winds might lead to a downward revision of the mass-loss rate (Moffat & Robert 1994), this would have important implications for evolutionary models of massive stars (Maeder 1991). Recently, some attempts have been made to relax certain assumptions of the standard model (Hillier 1996, and references therein), and spectral analysis using clumped wind models has been attempted (Schmutz 1997; Hillier & Miller 1998).

The difficulty in establishing realistic, inhomogeneous wind models is that clues about the degree of clumping have mainly come from indirect observational methods. For example, continuum-emission excess in the infrared and radio, which is interpreted as excess free-free emission due to wind overdensities (Lamers & Waters 1984), was observed in 18 early-type stars (Runacres & Blomme 1996). Though models of inhomogeneous winds were shown to reproduce the IR and radio excess well (Blomme & Runacres 1997), only limited constraints on the *detailed* density structure could be obtained, since observations mostly depend on the *global* effects of clumping. Stochastic variations in polarization and photometry of single WR stars were also interpreted in terms of residuals from a clumped wind (Robert et al. 1989). Other examples include measures in the intensity of the electron-scattering wings in some WR emission lines (Hillier 1991), the relative intensity of the IR lines of He I and He II (Nugis & Niedzielski 1995), and  $\lambda$ -dependence in the secondary eclipse in V444 Cyg (Cherepashchuk, Khaliullin, & Eaton 1984).

Although we can directly observe details in the clumpy structure of wind-blown bubbles around Wolf-Rayet stars (see Marston 1997), we cannot yet directly resolve regions close to the star, where emission lines are formed and the wind is presumably driven by the intense radiation field. In the near future, it might be possible to resolve this wind region in  $\gamma^2$  Vel, the closest WR star at  $\sim 250$  pc (van der Hucht et al. 1997; Schaerer, Schmutz, & Grenon 1997), using optical interferometric imaging techniques (see Vakili et al. 1997). Still, most WR stars will remain out of reach, at least initially.

Another technique that can provide limited resolution of the inhomogeneous structure of the wind, and that is independent of the distance, is high-resolution spectroscopy of broad emission lines. Because of the large Doppler shifts induced by the high wind velocity, regions in the wind having large differences in their line-of-sight velocities can be resolved on the emission-line spectrum. Early observations showed rapidly fluctuating features in the broad C III  $\lambda 5696$  emission-line profile of the WC7 component in the binary star HD 152270 (Schumann & Seggewiss 1975). These were interpreted as spectroscopically resolved, moving clouds or knots in the expanding wind. Later, high-resolution spectroscopic monitoring of the He II  $\lambda 5412$  emission line in the WN6 star HD 191765 revealed many narrow, moving emission features superposed on the emission-line profile (Moffat et al. 1988). These appeared to be the trace signature of clumps being accelerating along with the wind and emitting for a few hours as they passed through the line-emission region (LER). Extensive monitoring of nine WR stars of various subtypes showed this phenomenon to be present in each star observed (Robert 1992, 1994), and to be apparently stochastic. Similar, but periodic, LPVs were also observed in some apparently single stars,

e.g., in HD 191765 (Vreux et al. 1992; McCandliss et al. 1994) and in EZ CMa (Robert et al. 1992; St-Louis et al. 1995; Morel, St-Louis, & Marchenko 1997). It is suspected that these periodic variations are linked either to the presence of a compact companion or to the rotation of global wind structures. However, whereas such a periodic behavior is observed in only a few stars, stochastic variations seem to be present in every WR star observed so far.

A phenomenological model has been suggested to explain the LPV patterns in terms of local overdensities (termed “blobs” or “clumps”) in WR winds, as being related, e.g., to compressible, supersonic turbulence (Robert 1992; Moffat et al. 1994). Each clump presumably follows the general wind expansion, giving rise to one emission-line subpeak as it moves in, through, and out of the LER. A similar inhomogeneous wind model had previously been investigated (see Antokhin et al. 1992) in relation to deviations in the shape of an emission-line profile for a clumped wind. A review of the simultaneous photometric, spectroscopic, and polarimetric variations expected from such a clumped wind model has been presented elsewhere (Brown et al. 1995).

In the first paper of this series (Lépine, Moffat, & Henriksen 1996, hereafter Paper I) we performed a preliminary analysis of LPVs in emission lines of WR stars using the clumped-wind hypothesis as a working model. We investigated the effects on the LPV patterns of a hierarchy of inhomogeneous elements, which might result from the presence of self-structured chaos (e.g., compressible turbulence) in the wind (Robert 1994; Henriksen 1994). This involved a study of the LPVs in a static situation (i.e., snapshots of the emission line).

In this second paper, we investigate the LPV patterns in a more general way, in terms of a complete, phenomenological model of radially propagating, discrete wind elements. We first present a database that comprises sets of high-resolution spectra of optical emission lines from nine WR stars (§ 2). Our phenomenological formalism, which allows for a simplified but general description of the inhomogeneous structure from a WR wind, is then presented (§ 3). We use this working model to generate synthetic spectral time series, which are analyzed in order to determine which information can be obtained from the LPV patterns (§ 4). We are helped in this by the introduction of two numerical tools that provide a systematic analysis of the LPV pattern. We perform a comparative analysis between the data and the simulations, and obtain various constraints on the inhomogeneous wind structure of the WR stars in our sample. The results are discussed in § 5. A summary is presented in the final section (§ 6).

## 2. SPECTROSCOPIC OBSERVATIONS

A set of high signal-to-noise ratio ( $S/N > 200$ ), high-resolution ( $\lambda/\Delta\lambda \sim 30,000$ ) spectra of emission lines from nine WR stars was obtained from two observing runs at the Canada-France-Hawaii Telescope (CFHT) in 1987 and 1988 and one at the European Southern Observatory (ESO) in 1989. Reduction and preliminary analysis was carried out by C. Robert as part of her Ph.D. thesis (Robert 1992). Basic characteristics of the selected targets are presented in Table 1. The CFHT spectra cover the optical region around the C III  $\lambda 5696$  line for the WC stars WR 135, WR 137, and WR 140, and around the He II  $\lambda 5411$  line for the WN stars WR 134, WR 136 and WR 138. The ESO spectra of stars WR 40,

TABLE 1  
SAMPLE OF WOLF-RAYET STARS OBSERVED

HD	WR <sup>a</sup>	Subtype	Orbital Period (yr)	$v_{\infty}$ <sup>b</sup> (km s <sup>-1</sup> )	Number of Spectra	S/N <sub>cont</sub>
96548 .....	40	WN8	...	975	16	350
164270 .....	103	WC9	...	1190	30	210
165763 .....	111	WC5	...	2415	28	150
191765 .....	134	WN6	...	1905	36	190
192103 .....	135	WC8	...	1405	26	180
192163 .....	136	WN6	...	1605	26	200
192641 .....	137	WC7+OB	12.6 <sup>c</sup>	1885	25	240
193077 .....	138	WN5+OB	4.2 <sup>d</sup>	1345	18	230
193793 .....	140	WC7+O4...5	7.94 <sup>e</sup>	2900	23	380

<sup>a</sup> WR number from the van der Hucht et al. 1981 catalog.

<sup>b</sup> Terminal wind velocities from Prinja, Barlow, & Howarth 1990.

<sup>c</sup> From Williams et al. 1996.

<sup>d</sup> From Annuk 1990.

<sup>e</sup> From Williams et al. 1990.

WR 103, and WR 111, cover a broader range with several emission lines (5200–5900 Å), but here we chose to study the same lines in each case as observed at CFHT, since these lines are the strongest isolated emission lines in the spectra of WC and WN stars. The temporal resolution and coverage (one spectrum every hour or so over an interval of  $\sim 8$  hr on each of three or four consecutive nights) make these spectral time series well suited for a comprehensive study of the LPVs on short timescales.

We present a compact display of the observed LPVs: time-wavelength gray-scale plots of the residuals after subtracting the mean line profile are shown in Figures 1, 2, and 3. These clearly reveal the presence of moving spectral features (subpeaks). The most apparent subpeaks have full widths at half-maximum (FWHMs) ranging from  $\sim 2$ –10 Å, with a typical amplitude of about 2%–8% of the line intensity. Residuals show subpeaks with positive (negative) amplitudes, which most likely indicate excess (lack) of emission. Absorption is unlikely, since subpeaks are exclusively observed in the spectral range spanned by the line-emission profile (Robert 1992). Subpeaks systematically move from line center toward line edges (Moffat et al. 1988; Robert 1992). This behavior rules out both nonradial pulsations, or any rotation/orbital motion hypothesis, since one-half of the subpeaks on average would then be expected to move toward the line center. Rather, these data are consistent with wind features accelerated outward along radial trajectories.

The central wavelength of a subpeak corresponds to the mean line-of-sight velocity of one local wind feature (via the Doppler effect). The subpeak width presumably reflects a dispersion in velocity within the feature. Such internal velocity dispersions may arise from thermal or turbulent motions, but they may also arise from a systematic velocity gradient throughout the feature (e.g., from a shock discontinuity). Subpeaks near the edges on the emission-line profile have the largest apparent line motion (i.e., line-of-sight acceleration), whereas subpeaks near the center appear to be almost stationary. This can be naturally explained as a consequence of the radial motion of wind features. With line-of-sight velocity  $\xi = v\mu$ , where  $\mu = \cos(\theta)$  is the projection factor relative to the line of sight ( $\theta = 0$ ), one sees that a radial motion having  $\mu = \text{const}$  implies a spectral motion  $\dot{\xi} = \dot{v}\mu$ . In a shelllike region centered on the

star, the wind has approximately constant radial velocity  $v$  and acceleration  $\dot{v}$ , which yields  $\dot{\xi} \propto \xi$ , similar to what is observed.

On the gray-scale plots in Figures 1, 2, and 3, the eye catches what appear to be a few moving subpeaks. It is tempting to assume each of these apparent features to arise in a single wind event (cloud or clump). It then appears possible to enumerate how many clump events instantaneously occur in the LER. Unfortunately, this is an overly simplistic interpretation of the data. In Paper I, we have shown that the few apparently individual subpeaks uncovered either by eye or by any other kind of structure identifier (such as multi-Gaussian profile fitting), may actually result from the sum of a large number of independent wind events. Only a few features actually appear because of superposition and blending effects. Therefore, the characteristics of apparent subpeaks extracted from the data can be biased, because they depend on the way in which subpeaks superpose in line-of-sight velocity space. This is why we have introduced numerical tools, such as the wavelet transform, which analyze the LPV pattern as a whole instead of a few apparently independent components.

Wavelet analysis is analogous to a windowed Fourier transform in that it yields simultaneous information on both the scale and the location of features in a signal. We have already discussed the advantages of the wavelet transform over the Fourier transform (see Paper I). We provide in Appendix A a brief review of our wavelet analysis method. One powerful tool is the wavelet spectrum, which is like a multiscale analyzer. We present in Figures 1, 2, and 3 the mean wavelet spectrum  $\langle \tilde{R}(\xi, \sigma_{\xi}) \rangle$  of the residual spectra from each star. The wavelet spectra show striking patterns that can be interpreted as consisting of two components: (1) a more or less uniform response over location  $\xi$ , which gradually decreases from small to medium scale  $\sigma_{\xi}$ , on which is superposed (2) a triangular pattern with maximum response near  $\sigma_{\xi} \sim 10^2$  km s<sup>-1</sup> (except for WR 134, where the maximum is nearer to  $\sigma_{\xi} \sim 10^{2.5}$  km s<sup>-1</sup>) and centered on  $\xi = 0$ . The first component is the wavelet response to instrumental noise, which is uniform over the spectrum and yields the highest response at the smallest scales (pixel-to-pixel variation). The second component is the wavelet response to intrinsic LPVs, as evidenced from the fact that the response correlates strongly with the

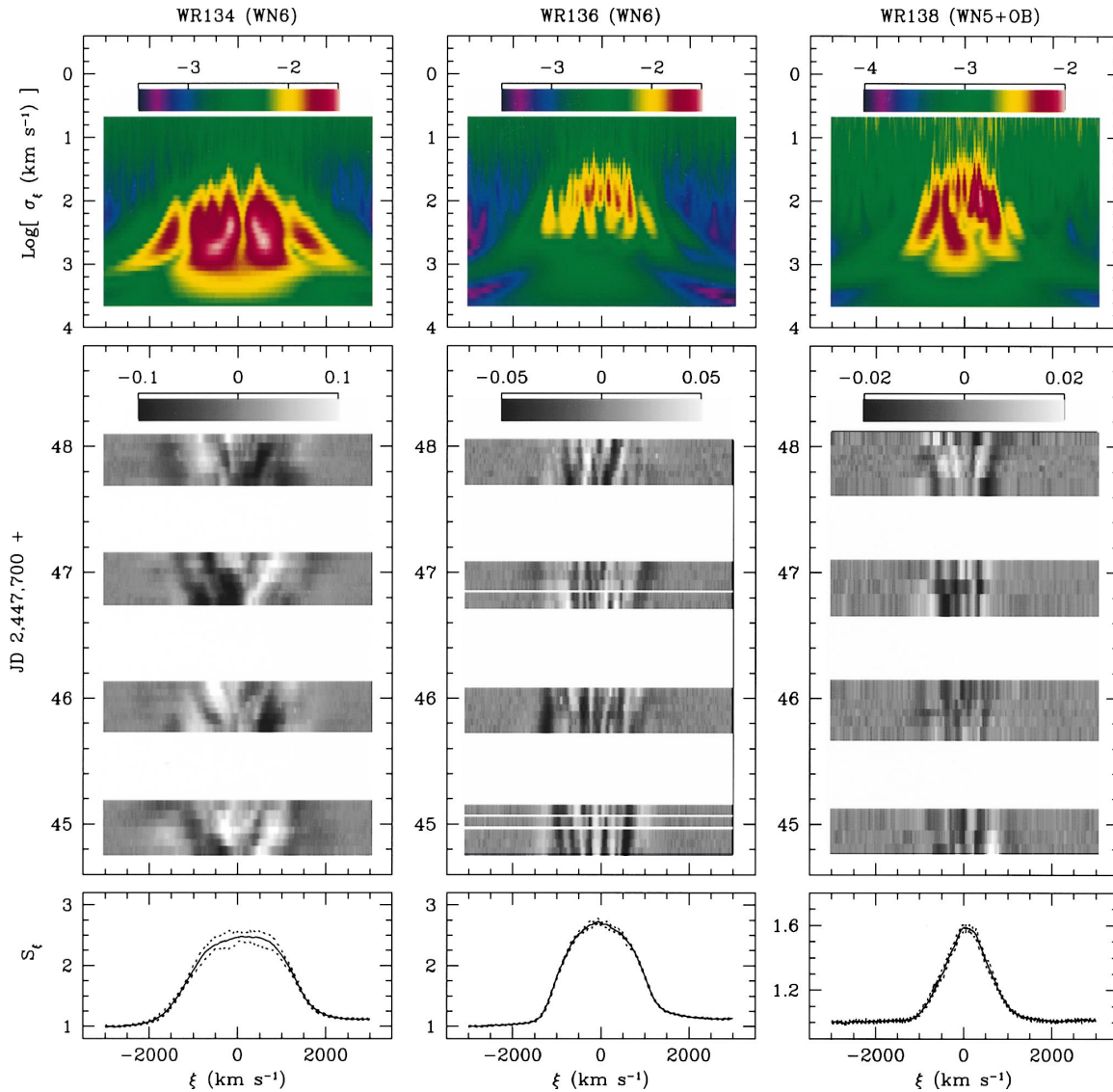


FIG. 1.—Plots of the LPVs observed in HD 191765 (= WR 134), HD 192163 (= WR 136), and HD 193077 (= WR 138). *Bottom panels*: Minimum, mean, and maximum measured values in the intensity in the He II  $\lambda 5411$  emission line for the whole observing run. *Center panels*: Time-resolved plots of the residuals after subtracting off the mean profile. *Color displays*: Wavelet spectrum from each time series. The wavelet spectrum identifies the typical location ( $\xi$ ) and scale ( $\sigma_\xi$ ) of the variable features in the LPVs. Note the outstanding behavior of WR 134, where the variable subpeaks are broader and a 2.3 day period occurs. Narrow subpeaks in the other stars appear to be stochastic.

emission-line profile and shows up on scales that are much larger than pixel-to-pixel variations.

The mean wavelet spectra provide clear evidence that the scale (width) of emission subpeaks depends on their location on the line; LPVs are made up of narrow subpeaks near the line center and broader ones near the edges. This behavior shows up especially well for the broadest emission lines (see WR 140). We note that the location where the narrowest intrinsic subpeaks are found coincides with  $\xi = 0$ . The pattern is also symmetrical around  $\xi = 0$ , indicating that the width of a subpeak does not depend on the sign of its line-of-sight velocity.

The general, multiscale properties of LPVs can be studied with the mean wavelet power spectrum. We have plotted in Figure 4 the mean wavelet power spectrum  $\langle \tilde{R} \rangle_{\text{LPV}}$  of the residuals averaged over the spectral domain  $\xi$  (see Appendix A). The maximum in  $\langle \tilde{R}(\sigma_\xi) \rangle_{\text{LPV}}$  yields an approximate measure for the mean line-of-sight velocity dispersion  $\overline{\sigma_\xi}$  of LPVs subpeaks. Most stars show a maximum in the range

$80 < \sigma_\xi < 150 \text{ km s}^{-1}$ . Stars WR 134 and WR 40 show broader features, with  $\overline{\sigma_\xi} \simeq 350 \text{ km s}^{-1}$ . We suspect that the broad subpeaks in WR 40 might result from variations in the whole line profile that can be confused, on residual spectra, with broad subpeaks having the width of the emission line. In any case, the wavelet spectrum of WR 40 in Figure 4 suggests the occurrence of narrow features on a scale similar to that found in other stars. On the other hand, the LPVs in WR 134 seem to be dominated by broad subpeaks; there is no clear evidence for a distinct population of narrow subpeaks. Thus, WR 134 appears to be a special case. Indeed, whereas observations suggest that LPVs in the other WR stars are stochastic, recurrence in the LPV patterns have been detected for WR 134 (McCandliss et al. 1994), confirmed and interpreted as being related to the rotation of a structured wind (Morel et al. 1999).

We note that the small-scale behavior of  $\langle \tilde{R}(\sigma_\xi) \rangle_{\text{LPV}}$  depends on the observing run. In the first CFHT run (WR 134, WR 136, and WR 138), the wavelet power in the range

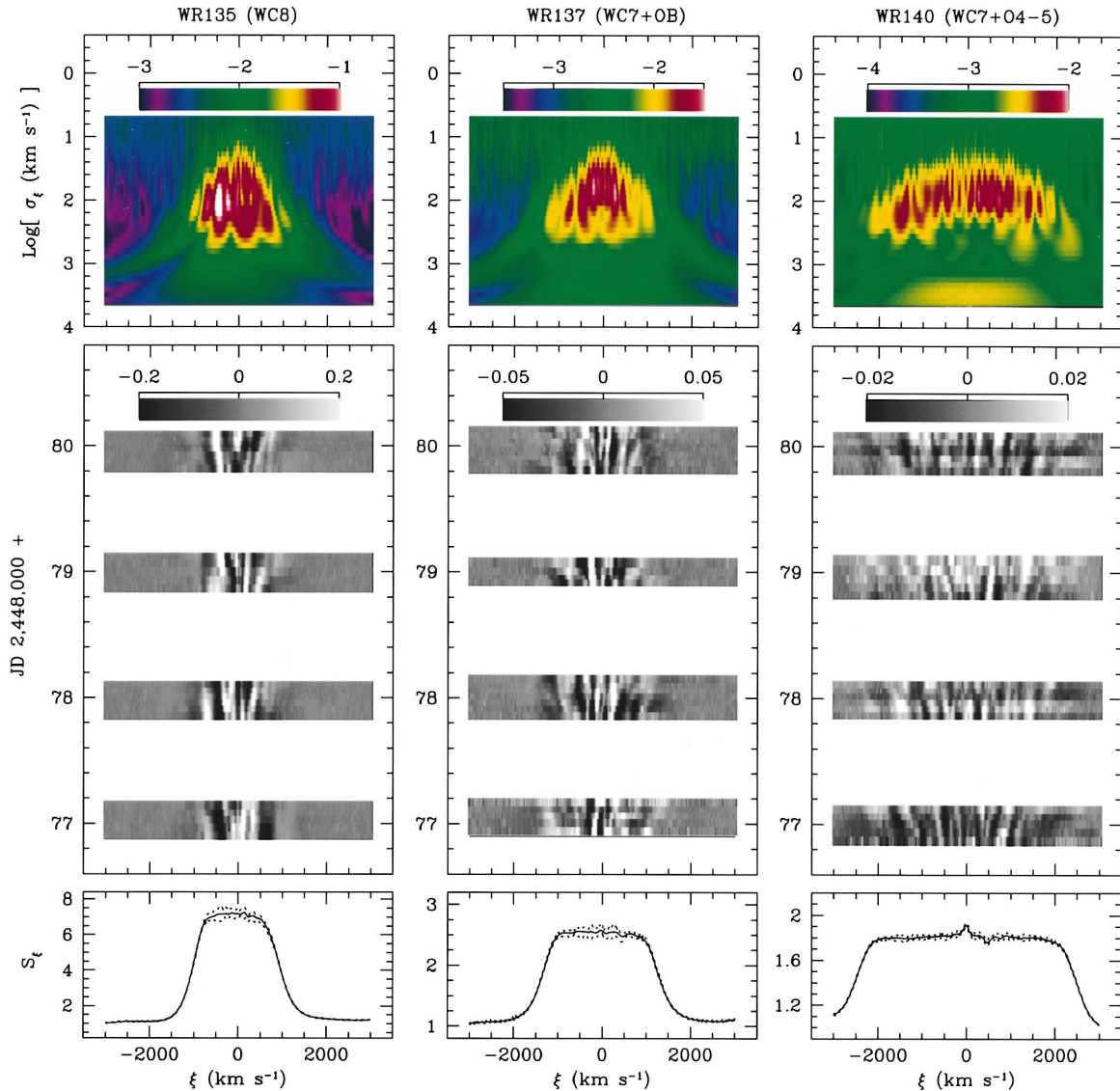


FIG. 2.—As in Fig. 1, but of the LPVs observed in the C III  $\lambda 5696$  emission line in HD 192103 (= WR 135), HD 192641 (= WR 137), and HD 193793 (= WR 140). One can see that subpeaks tend to propagate from lower to higher  $|\xi|$ . Note how the number of apparent subpeaks increases with the emission line width, an artifact that is explained in § 4.1.

$0.5 < \log [\sigma_\xi \text{ (km s}^{-1}\text{)}] < 1.2$  is more or less uniform, whereas in the second run (WR 135, WR 137, and WR 140), the wavelet power increases proportionally with  $\sigma_\xi$ . It appears that the scaling properties of the CFHT instrumental noise are epoch dependent. In the ESO run (WR 40, WR 103, and WR 111), there is a sharp drop in power below  $\log [\sigma_\xi \text{ (km s}^{-1}\text{)}] \sim 0.8$ ; this arises because a smoothing procedure was applied to this particular data set in the reduction procedure, to remove a contaminating high-frequency signal (Robert 1992).

Our wavelet analysis technique has some advantages over other methods for the identification of intrinsic variability, such as the temporal variance spectrum (TVS) technique (Fullerton 1990; Robert 1992). The TVS compares the variability at each pixel with that expected from instrumental noise, accounting for the quality of each individual spectrum. However, while TVS works on pixel elements individually, wavelet analysis separates the variable features according to their scale (in wavelength space) and thus can make use of the fact that some intrinsic subpeak features

may occupy several neighboring pixels. The wavelet spectrum may thus effectively separate the generally small-scale instrumental noise from the intrinsic large-scale features, yielding a straightforward detection of the latter.

### 3. PHENOMENOLOGICAL, CLUMPED WIND MODEL

#### 3.1. Discrete Wind Emission Elements

The intrinsic, stochastic subpeaks can be described as statistical fluctuations arising in a distribution of discrete emission features. The amplitude of the fluctuations should depend on the number of discrete elements as well as on their individual flux. Assume that the line emission can be represented as arising in a finite number  $N_e$  of “discrete wind emission elements” (DWEEs). Line emission from a single DWEE arises as the associated wind feature passes through the LER, where the ionization balance is such as to stimulate the emission from the given atomic transition. The LER is expected to span some well-defined range from the underlying WR star. Line variability is expected to



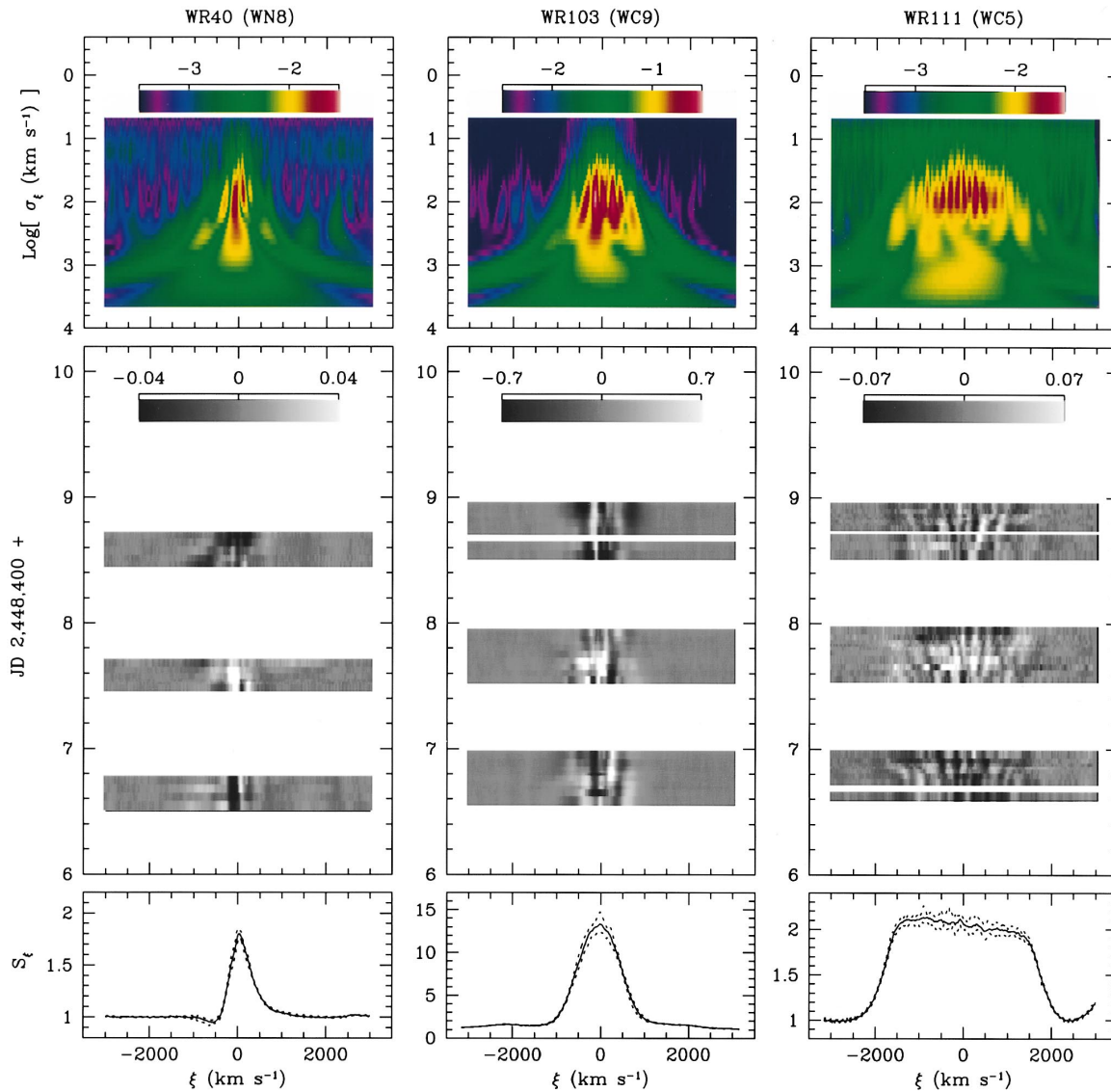


FIG. 3.—As in Figs. 1 and 2, but of the LPVs observed in the He II  $\lambda 5411$  emission line in HD 96548 (= WR 40) and in the C III  $\lambda 5696$  emission line in HD 164270 (= WR 103) and HD 165763 (= WR 111). The wavelet spectra reveal that, in all nine WR stars, the scale  $\sigma_\xi$  of variable subpeaks is smaller near the line center  $\xi = 0$  and larger near the edges.

occur because the discrete wind elements will successively move in and out of this LER. Our model of LPVs is therefore very simple: every DWEE has an assigned location in the wind; as this location changes (according to the wind velocity law) the DWEE enters the LER and yields a discrete subpeak in the emission-line profile; this subpeak vanishes as the DWEE leaves the LER. This is sufficient to reproduce the observed LPV patterns with reasonable fidelity.

Let  $[r_i, \mu_i, \phi_i]$  be the coordinates of the  $i$ th DWEE, in a spherical coordinate system centered on the star, with  $\mu_i = \cos \theta_i$ . We assume that the wind is radially expanding and that the expansion follows a monotonically increasing velocity law  $v(r)$ . It simplifies things to calculate the problem in the directly observable bulk wind velocity space and use the coordinates  $[v_i, \mu_i, \phi_i]$ , with  $v_i = v(r_i)$ . Let  $s_i = s_i(\xi)$  be the spectral emission (subpeak) arising from the  $i$ th DWEE, where we use the line-of-sight Doppler velocity  $\xi \equiv \lambda_0^{-1}(\lambda - \lambda_0)c$ , with  $\lambda_0$  the rest wavelength of the line radiation and

$c$  the speed of light. We assume that  $s_i(\xi)$  is of the form

$$s_i(\xi) = \frac{F_i}{\sigma_{\xi i} \sqrt{\pi}} \exp \left( -\frac{(\xi - \xi_i)^2}{\sigma_{\xi i}^2} \right). \quad (1)$$

Here,  $F_i$  is the integrated emission-line flux from the DWEE;  $\xi_i$  and  $\sigma_{\xi i}$  are the spectral location and the width of the subpeak feature, respectively.

The parameter  $\xi_i$  corresponds to the mean line-of-sight velocity of the emitting material in the DWEE, i.e.,  $\xi_i = \mu_i v_i$ . Since the DWEE is moving, it is implicitly assumed that  $v_i = v_i(t)$ . The value for  $v_i$  at any given time can be obtained from the wind velocity law  $v = v(r)$  (see § 3.2 below). Since we assume that DWEEs move only radially,  $\mu_i$  is a constant. The velocity dispersion  $\sigma_{\xi i}$  reflects the motion of atoms associated with the DWEE. This includes thermal and turbulent motions, as well as possible systematic velocity gradients within the element. Values for  $\sigma_{\xi i}$  might vary with distance from the star, and the velocity

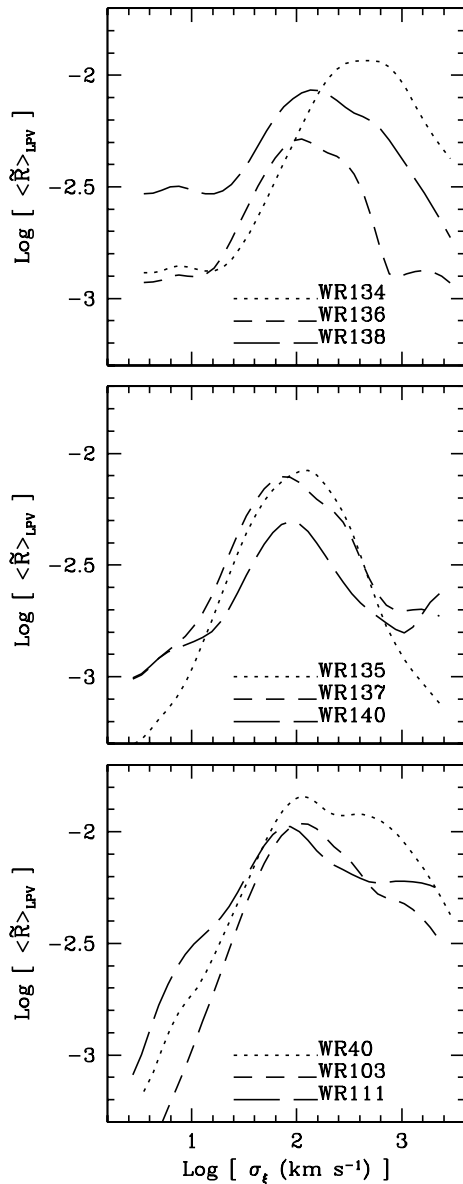


FIG. 4.—Mean wavelet power spectrum  $\langle \tilde{R}(\sigma_{\xi}) \rangle_{\text{LPV}}$  for all the spectral time series in our data set. All stars show a maximum at  $\sigma_{\xi} \approx 100 \text{ km s}^{-1}$ , except for WR 134, which has a maximum near  $\sigma_{\xi} \approx 350 \text{ km s}^{-1}$ . The width of the stochastic subpeaks is apparently independent of the star observed, but the periodic subpeaks in WR 134 are significantly broader. Note how the behavior of  $\langle \tilde{R}(\sigma_{\xi}) \rangle_{\text{LPV}}$  at small  $\sigma_{\xi}$  depends on the observing run, indicating variable noise quality and statistics.

dispersion might be anisotropic. As we will show (§ 3.3), the LER does not usually span a large domain in wind bulk velocity, and possible variations in  $\sigma_{\xi i}$  with depth can be neglected. However, we do need to consider possible anisotropic effects (§ 3.4).

The observed global emission-line profile  $S(\xi)$  will result from the combination of a large number  $N_e$  of DWEEs:

$$S(\xi) = \sum_{i=1}^{N_e} s_i(\xi). \quad (2)$$

We expect the resulting emission-line profile to be variable, depending on the mean number of DWEEs. An inhomogeneous wind with a very large  $\overline{N_e}$  should yield a line profile very close to that of a smooth wind, whereas a wind with a

small  $\overline{N_e}$  will result in high levels of variability. The patterns of LPVs, however, will be critically dependent on the wind velocity law and on the geometry of the LER, as well as on the statistical distribution of fluxes from individual DWEEs.

### 3.2. The Velocity Law

The velocity law describes the bulk motion of the accelerated wind material as a function of distance from the star. The most popular velocity law typically used in models of hot-star winds is the so-called  $\beta$ -law (Castor & Lamers 1979),

$$v(r) = v_{\infty} \left( 1 - \frac{R_*}{r} \right)^{\beta}, \quad (3)$$

which is given here in its simplest version, with  $v_{\infty}$  the terminal velocity of the wind and  $R_*$  some spatial dimension of the order of the stellar radius. This law is a parameterized generalization of a law that arises from the theory of radiation-driven winds (Castor, Abbott, & Klein 1975; the so-called CAK model). Different values of  $\beta$ , typically in the range  $[0.5, 4.0]$ , have been used in the literature for different models and stars.

In the approximation of point source stars, the CAK theory predicts a velocity law with  $\beta = 0.5$ . When finite disk effects are considered, the CAK theory yields  $\beta = 0.8$  (Friend & Abbott 1986). In modeling the winds of OB and WR stars, the velocity field is usually assumed to follow the  $\beta$ -law, but the value of  $\beta$  is left as a free parameter. A value of  $\beta \approx 1$  has been successfully used for models of stellar winds from OB stars (Puls et al. 1996), while observations of LPV subpeaks in WR winds suggest much larger values of  $\beta$  (Robert 1994). This is supported by recent spectral analysis of WR spectra with a clumped wind model (Schmutz 1997), which yields fits of the velocity law with  $\beta \approx 4-8$ .

The  $\beta$ -law yields an “acceleration law” in the form

$$a(r) \equiv \frac{dv}{dt} = v \frac{dv}{dr} = \frac{v_{\infty}^2}{R_*} \left( \frac{R_*}{r} \right)^2 \beta \left( 1 - \frac{R_*}{r} \right)^{2\beta-1}. \quad (4)$$

The acceleration  $a$  can also be expressed as a function of the local, bulk wind velocity  $v$ :

$$a(v) = \beta \frac{v^2}{R_*} \left[ \left( \frac{v}{v_{\infty}} \right)^{-1/2\beta} - \left( \frac{v}{v_{\infty}} \right)^{1/2\beta} \right]^2. \quad (5)$$

It turns out that the function  $\beta a(v)$  converges very fast for  $\beta \rightarrow \infty$  such that, for  $\beta > 1$ , we may use the approximation

$$\beta a(v) \simeq \lim_{\beta \rightarrow \infty} \beta a(v) = R_*^{-1} [v \ln(v/v_{\infty})]^2. \quad (6)$$

Figure 5 shows the  $a(r)$  and  $\beta a(v)$  functions for different values of the parameter  $\beta$ . One sees that the approximation in equation (6) yields values of  $\beta a(v)$  to better than  $\sim 5\%$  for all  $\beta \gtrsim 2$ . This result has important implications, because it means that unless there exists a reliable estimate of  $R_*$  (which is usually not the case for WR stars), it is not possible to determine  $\beta$  from the magnitude of the acceleration alone, since we have  $a(v) \propto \beta^{-1} R_*^{-1}$ . A measure of the wind acceleration as a function of the velocity, combined with a knowledge of  $v_{\infty}$ , yields only a constraint on  $\beta R_*$ . On the other hand, any large divergence from the very specific  $a(v)$  function rules out the  $\beta$ -law as an adequate representation of the motion of inhomogeneous wind features.

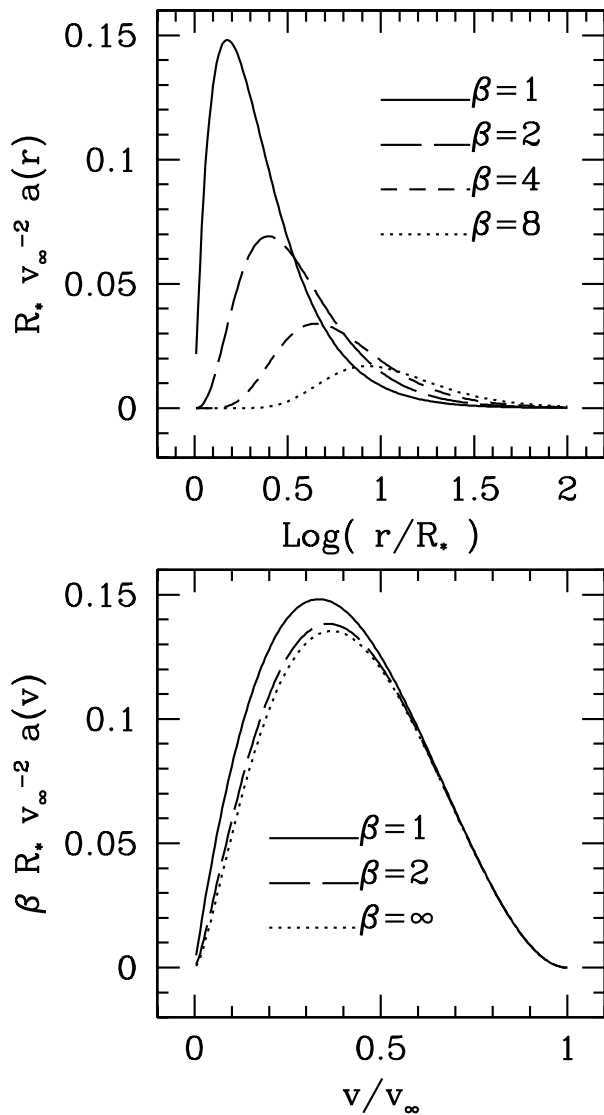


FIG. 5.—Illustration of the  $\beta$ -law, the commonly adopted velocity law used in hot star wind models. *Upper panel*: Dimensionless acceleration plotted as a function of radius. In velocity space, however, the  $\beta$ -law has the same general shape for all relevant values of  $\beta$  (*lower panel*). This is crucial in the interpretation of our data, since spectroscopy measures only events in velocity space.

### 3.3. Line Emission from DWEEs

The line flux  $F_i$  from each DWEE depends on its distance from the star or, equivalently, on its velocity  $v_i$ . The DWEE will be emitting line radiation while being accelerated through the LER. Letting  $F_i$  be the emission-line flux from a DWEE, we may write  $F_i = f_i f_e(v_i)$ , where  $f_e(v_i)$  is the dependence of the line flux with the location  $v_i$  of the DWEE in the wind and  $f_i$  is a constant that allows for the relative emission from that DWEE (no two are alike).

The most rigorous way to obtain  $f_e(v_i)$ , or more generally  $f_e(v)$ , would be to use reliable theoretical WR models. In standard models of WR winds, recombination-line emission in WR winds arises in concentric “shells,” whose depth and thickness depend on the particular line transition (see, e.g., Hillier 1988, 1989). The classical approach to obtaining an estimate of  $f_e(v)$  for one specific line transition would be to perform standard spectral analysis and derive  $\Phi_e(r)$ , the emission as a function of distance from the star, from which

one gets  $f_e(v) \simeq \Phi_e[r(v)]$ , where  $r(v)$  is obtained by inversion of the velocity law  $v(r)$ .

However, here we are interested in obtaining the most information from observations alone. It is possible to derive an approximate expression for the total line flux  $F_e(v)$  as a function of the radial velocity  $v$  from the shape of the emission-line profile (see Brown et al. 1997). The technique is based on the assumptions that the wind is roughly homogeneous, spherically symmetric, and optically thin. An emission-line profile can be imagined to consist of a sum of profiles arising from infinitesimally thin, concentric wind shells. It is easily shown that the emission  $dF$  of such a shell formed by wind material having a velocity between  $v$  and  $v + dv$  yields a spectral profile  $dS(\xi, v)$  in the form

$$dS(\xi, v) = \begin{cases} F_0 \frac{F_e(v)}{a(v)} dv, & -v < \xi < v \\ 0, & \text{otherwise,} \end{cases} \quad (7)$$

where  $a(v)$  is the “acceleration law” (see eq. [5]) and  $F_0$  is some normalization constant. The global line profile  $S(\xi)$  is the sum of all shells:

$$S(\xi) = \int_{v=0}^{v=v_\infty} dS(\xi, v). \quad (8)$$

It is possible to solve the inverse problem (see Brown et al. 1997) to obtain  $F_e(v)$  from the shape of the line profile  $S(\xi)$ :

$$F_e(v) \propto a(v) v^{-1} \left( \frac{dS}{d\xi} \right)_{|\xi|=v}. \quad (9)$$

This is equivalent to performing a “spherical deprojection” of the line emission, starting with the emission as a function of line-of-sight velocity  $\xi$  to obtain emission as a function of radial velocity  $v$ . We note that the observed  $F_e(v)$  is expected to deviate from the theoretical  $f_e(v) = \Phi_e[r(v)]$ , because  $F_e(v)$  is affected by the existence of “turbulent” motions, which tend to increase the apparent range of line emission in velocity space, whereas  $f_e(v)$  should reflect the extension of the LER in distance space only. Both sides of the emission line profile ( $\xi < 0$  and  $\xi > 0$ ) can in principle be used to estimate  $F_e(v)$ . However, the redshifted side of the emission line ( $\xi > 0$ ) may be affected by stellar occultation (see Ignace et al. 1998), and the blueshifted side may also be affected by P Cygni-type absorption. We therefore use either the blueshifted or redshifted side of the line, depending on whether these biases are assumed to be significant or not.

In Figure 6 we plot  $F_e(v)$ , as obtained from equation (9), for the emission lines of the WR stars in our sample, using  $a(v)$  from equation (6) as the velocity law. We then fitted the  $F_e(v)$  using a Gaussian-like function, which appears to be quite appropriate:

$$F_e(v) \propto \exp \frac{-(v - v_e)^2}{\Delta v_e^2}, \quad (10)$$

with the free parameters  $v_e$ , the velocity regime where maximum emissivity occurs, and  $\Delta v_e$ , the extension of the LER in velocity space. Although this parameterization is, at best, a crude approximation of the actual emissivity function, it serves our purpose reasonably well here, since we are mainly interested in the approximate size of the region where most of the emission occurs, and not in the detailed line emission, e.g., in regions closer to the star where it is



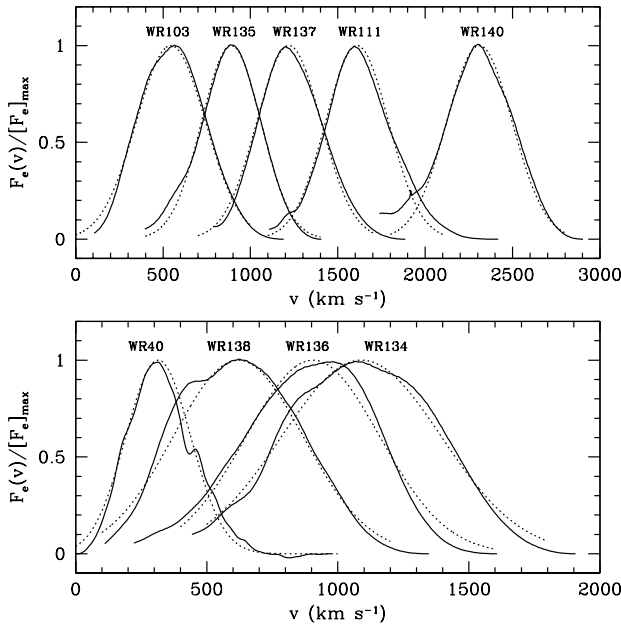


FIG. 6.—Deprojected emission function  $F_e(v)$  for the WR stars in our sample, obtained with the method discussed in § 3.3. This yields the relative emission from discrete wind elements as a function of their radial velocity. Dotted lines show the best-fit Gaussian profiles, whose parameters are listed in Table 2. The mean emission-line profiles (see Figs. 1, 2, and 3) were smoothed with a low-pass filter before computation of  $F_e(v)$ , in order to reduce instrumental noise effects. Normalization to the maximum value  $[F_e]_{\max}$  facilitates the comparison between stars.

relatively small. Best fits are plotted in Figure 6, and results are listed in Table 2. For the C III  $\lambda 5696$  line (WC stars), the values obtained should be reliable estimates of the size and extension of the LER (within the validity of the  $\beta$ -law), since the line is optically thin. On the other hand, the He II  $\lambda 5411$  line in the WN stars is likely not to be optically thin, which means that the estimated size and location of the LER will be biased by the fact that optically thick lines tend to be naturally rounded (Castor 1970). In this case,  $\Delta v_e$  will overestimate the actual extension in velocity space of the LER. As it turns out, the  $\Delta v_e$  obtained from the WN stars are significantly larger (except in the case of the WN8 star WR 40) than those measured in the WC stars.

TABLE 2

WIND PROPERTIES FROM THE SHAPE OF THE EMISSION-LINE PROFILES

WR Star	Transition	EW (km s <sup>-1</sup> )	$v_e$ (km s <sup>-1</sup> )	$\Delta v_e$ (km s <sup>-1</sup> )
WR 40 .....	He II $\lambda 5411$	-460	315 ± 10	175 ± 10
WR 103 .....	C III $\lambda 5696$	-15500	545 ± 10	280 ± 10
WR 111 .....	C III $\lambda 5696$	-3580	1610 ± 10	255 ± 10
WR 134 .....	He II $\lambda 5411$	-3860	1090 ± 10	430 ± 20
WR 135 .....	C III $\lambda 5696$	-13040	890 ± 10	240 ± 10
WR 136 .....	He II $\lambda 5411$	-3480	905 ± 10	360 ± 15
WR 137 .....	C III $\lambda 5696$	-4410	1220 ± 10	260 ± 10
WR 138 .....	He II $\lambda 5411$	-740	620 ± 10	350 ± 15
WR 140 .....	C III $\lambda 5696$	-4090	2310 ± 10	265 ± 10

NOTES.—The line equivalent width (EW) is translated into km s<sup>-1</sup> units, as the line is plotted in projected velocity space  $\xi$ . Parameters  $v_e$  and  $\Delta v_e$  are derived from the shape of the line profile and correspond to the mean wind velocity of line-emitting material and the emission-line broadening (dispersion in velocity space), respectively.

Since the velocity dispersion  $\Delta v_e$  reflects the radial extension of the LER in bulk wind velocity space as well the turbulent motions within the LER region, we use the relation

$$\Delta v_e \simeq \sigma_{v_e} + \sigma_{v_r}, \quad (11)$$

where  $\sigma_{v_r}$  is a measure of the radial “turbulent” motions within the LER, and  $\sigma_{v_e}$  is the spatial extension of the LER translated in bulk wind velocity space. We may estimate  $\sigma_{v_r}$  from the widths of LPV subpeaks, assuming these to be a reliable measure of local velocity dispersions in the wind. The effective emission function  $f_e(v)$  for individual DWEEs becomes

$$f_e(v) \propto \exp \frac{-(v - v_e)^2}{\sigma_{v_e}^2}. \quad (12)$$

As we will show in § 4.4, we can obtain an independent estimate of  $\sigma_{v_e}$  from an analysis of LPV patterns. This will allow us to verify the consistency of  $\sigma_{v_e}$  as estimated from the shape of the emission-line profile.

DWEEs are assumed not to have the same relative emission. For practical purposes, and inspired by previous studies (see Paper I), we will use a statistical power-law distribution in the form  $n(f)df \sim f^{-\alpha} df$  and let the individual fluxes  $f$  be in a range  $f_0 < f < \eta f_0$ , with  $\eta > 1$ . For  $F_e$  the mean total flux in the line emission and  $N_e$  the mean number of DWEEs in the LER (i.e., clumps in the  $v_e - \sigma_{v_e} < v < v_e + \sigma_{v_e}$  velocity regime, where most of the flux is found), we get the statistical distribution function,

$$n(f) = K_f \left( \frac{f}{f_0} \right)^{-\alpha}, \quad (13)$$

where  $K_f$  and  $f_0$  are functions of the parameters  $F_e$ ,  $N_e$ ,  $\alpha$ , and  $\eta$ . These are determined with the relations

$$N_e = \int_{f_0}^{\eta f_0} n(f) df \quad (14)$$

and

$$F_e = \int_{f_0}^{\eta f_0} f n(f) df. \quad (15)$$

The flux distribution is therefore defined by four independent parameters ( $F_e$ ,  $N_e$ ,  $\alpha$ , and  $\eta$ ). Of these, the total line flux  $F_e$  is determined by the emission-line equivalent width. The distribution therefore uses three free parameters ( $N_e$ ,  $\alpha$ , and  $\eta$ ).

### 3.4. Anisotropy

The wavelet analysis has revealed that the widths of emission subpeaks depend on their location on the line profile. This suggests that DWEEs have anisotropic velocity dispersions. We model this anisotropy by expressing the velocity dispersion of DWEEs as a vector  $\sigma_v$ :

$$\sigma_v(\mathbf{r}) = \sigma_{v_r} \hat{\mathbf{r}} + \sigma_{v_\theta} \hat{\boldsymbol{\theta}} + \sigma_{v_\phi} \hat{\boldsymbol{\phi}}, \quad (16)$$

where  $\sigma_{v_r}$ ,  $\sigma_{v_\theta}$ , and  $\sigma_{v_\phi}$  are the velocity dispersions in the radial, latitudinal, and longitudinal directions  $\mathbf{r}$ ,  $\boldsymbol{\theta}$ , and  $\boldsymbol{\phi}$ , respectively. The scalar, line-of-sight velocity dispersion  $\sigma_{\xi i}$  of one DWEE will be

$$\sigma_{\xi i} = \sqrt{\mu_i^2 \sigma_{v_r}^2 + (1 - \mu_i^2) \sigma_{v_\theta}^2}, \quad (17)$$

where we assume  $\sigma_{v_\theta} = \sigma_{v_\phi}$ . Consider a spherical shell confining a region of approximately constant wind expansion velocity  $v_e$ . Within this region, we get a relation between  $\sigma_\xi$  and  $\xi$ , namely,

$$\sigma_\xi(\xi) = \sqrt{\frac{\xi^2}{v_e^2} (\sigma_{v_r})^2 + \left(1 - \frac{\xi^2}{v_e^2}\right) (\sigma_{v_\theta})^2}. \quad (18)$$

Moffat & Robert (1992) already surmised this in their preliminary analysis of emission-line subpeaks of the WR star WR 140, supporting evidence for anisotropic local velocity dispersion.

Similarly, we may allow for the emission from individual DWEs to be anisotropic as well. This can happen because, e.g., of optical depth effects. Following the same reasoning as for  $\sigma_\xi$ , we will now write the flux  $F_i$  from the  $i$ th DWE as

$$F_i = f_i f_e(v_i) \sqrt{\mu_i^2 f_r^2 + (1 - \mu_i^2) f_\theta^2}, \quad (19)$$

where  $f_r$  and  $f_\theta$  define escape probabilities in the directions  $r$  and  $\theta$ . In the optically thin case, we use  $f_r = f_\theta = 1$ , whereas the optically thick case can be modeled with  $f_r \neq f_\theta$ .

#### 4. COMPARATIVE ANALYSIS

##### 4.1. Spectroscopic Resolution of Wind Elements

The large velocities of spherically expanding WR winds, combined with the Doppler effect, generate very broad line profiles. Spectroscopy therefore allows the observer to resolve parts of the wind in emission-line radiation, i.e., to observe wind regions having different line-of-sight bulk velocities separately. However, a practical limit is set by

local velocity dispersions (such as atomic thermal motions or turbulence), which blend the emission from regions having different spatial locations, but similar line-of-sight velocities. Let an emission line arise in a spherically expanding LER with mean radial velocity  $v_e$ , and mean local line-of-sight velocity dispersion  $\overline{\sigma_\xi}$  (see § 3). We define the spectroscopic wind resolving power  $R_w \equiv v_e \overline{\sigma_\xi}^{-1}$ . Higher values of  $R_w$  mean that a larger number of wind regions can be resolved with spectroscopy. The best results should therefore be obtained for winds having large bulk velocities and relatively small turbulent motions.

We present in Figure 7 simulations of LPV patterns obtained from the phenomenological model presented in § 3. Values of the parameters used in each simulation are listed in Table 3. The first series (SIM 1, SIM 2, SIM 3) shows how the LPV pattern is affected by a change in  $v_e$ . All three simulations used exactly the same distribution of DWEs; only the values of  $v_\infty$  and  $R_*$  were adjusted. One notices that the number of apparent subpeaks is proportional to the width of the line (i.e., to  $v_e$ ). Note how the apparent subpeaks in SIM 1 break up into many resolved components in SIM 3. Similar effects on the LPV patterns can be obtained by varying  $\overline{\sigma_\xi}$ . One example is shown by the other three simulations (SIM 4, SIM 5, SIM 6) where, again, the same spatial distribution of DWEs was used, but with different values for their  $\sigma_\xi$ .

In previous studies of LPV patterns in WR emission lines (Robert 1994), it was found that the number of subpeaks observed on the emission line was proportional to the terminal velocity  $v_\infty$  of the wind. In the light of our current investigation, this correlation finds an easy explanation.

TABLE 3  
PARAMETERS OF THE SIMULATIONS

Simulation Number	$R_*$ ( $R_\odot$ )	$v_\infty$ (km s <sup>-1</sup> )	$\beta$	$v_e$ ( $v_\infty$ )	$\sigma_{v_e}$ ( $v_\infty$ )	$F_e$ (km s <sup>-1</sup> )	$N_e$	$\alpha$	$\eta$	$\sigma_{v_r}$ (km s <sup>-1</sup> )	$\sigma_{v_\theta}$ (km s <sup>-1</sup> )	$f_r/f_\theta$
SIM 1 .....	2.5	750	4	0.65	0.15	2000	10 <sup>3</sup>	4	10 <sup>4</sup>	200	75	1
SIM 2 .....	5	1500	4	0.65	0.15	2000	10 <sup>3</sup>	4	10 <sup>4</sup>	200	75	1
SIM 3 .....	10	3000	4	0.65	0.15	2000	10 <sup>3</sup>	4	10 <sup>4</sup>	200	75	1
SIM 4 .....	5	1700	4	0.65	0.10	2000	10 <sup>3</sup>	4	10 <sup>4</sup>	100	50	1
SIM 5 .....	5	1700	4	0.65	0.10	2000	10 <sup>3</sup>	4	10 <sup>4</sup>	200	100	1
SIM 6 .....	5	1700	4	0.65	0.10	2000	10 <sup>3</sup>	4	10 <sup>4</sup>	400	200	1
SIM 7 .....	5	2000	4	0.65	0.10	2000	10 <sup>4</sup>	2	10 <sup>3</sup>	200	100	1
SIM 8 .....	5	2000	4	0.65	0.10	2000	10 <sup>4</sup>	2	10 <sup>2</sup>	200	100	1
SIM 9 .....	5	2000	4	0.65	0.10	2000	10 <sup>4</sup>	2	10 <sup>1</sup>	200	100	1
SIM 10 .....	5	2000	4	0.65	0.10	2000	10 <sup>4</sup>	3	10 <sup>3</sup>	200	100	1
SIM 11 .....	5	2000	4	0.65	0.10	2000	10 <sup>4</sup>	4	10 <sup>3</sup>	200	100	1
SIM 12 .....	5	2000	4	0.65	0.10	2000	10 <sup>4</sup>	6	10 <sup>3</sup>	200	100	1
SIM 13 .....	5	2000	4	0.65	0.10	2000	10 <sup>2</sup>	3	10 <sup>3</sup>	200	100	1
SIM 14 .....	5	2000	4	0.65	0.10	2000	10 <sup>3</sup>	3	10 <sup>3</sup>	200	100	1
SIM 15 .....	5	2000	4	0.65	0.10	2000	10 <sup>5</sup>	3	10 <sup>3</sup>	200	100	1
SIM 16 .....	5	2000	4	0.65	0.10	2000	10 <sup>3</sup>	3	10 <sup>2</sup>	100	100	3
SIM 17 .....	5	2000	4	0.65	0.10	2000	10 <sup>3</sup>	3	10 <sup>2</sup>	130	65	3
SIM 18 .....	5	2000	4	0.65	0.10	2000	10 <sup>3</sup>	3	10 <sup>2</sup>	160	40	3
SIM 19 .....	5	2000	4	0.65	0.10	2000	10 <sup>3</sup>	3	10 <sup>2</sup>	100	100	1
SIM 20 .....	5	2000	4	0.65	0.10	2000	10 <sup>3</sup>	3	10 <sup>2</sup>	130	65	1
SIM 21 .....	5	2000	4	0.65	0.10	2000	10 <sup>3</sup>	3	10 <sup>2</sup>	160	40	1
SIM 22 .....	5	2000	4	0.65	0.10	2000	10 <sup>3</sup>	3	10 <sup>2</sup>	100	100	0.3
SIM 23 .....	5	2000	4	0.65	0.10	2000	10 <sup>3</sup>	3	10 <sup>2</sup>	130	65	0.3
SIM 24 .....	5	2000	4	0.65	0.10	2000	10 <sup>3</sup>	3	10 <sup>2</sup>	160	40	0.3

NOTES.— $R_*$ : wind velocity-law parameter (roughly stellar core radius);  $v_\infty$ : terminal wind velocity;  $\beta$ : velocity-law power index;  $v_e$ : location of the LER in wind-velocity space;  $\sigma_{v_e}$ : extension of the LER in wind velocity space;  $F_e$ : mean emission-line flux (equivalent width in units of projected Doppler velocity);  $N_e$ : mean number of DWEs in the LER;  $\alpha$ : power index in the statistical distribution of DWE fluxes;  $\eta$ : total range in the flux from individual DWEs;  $\sigma_{v_r}$ : velocity dispersion in the direction of propagation (radial);  $\sigma_{v_\theta}$ : velocity dispersion perpendicular to propagation; and  $f_r/f_\theta$ : escape probability ratio.

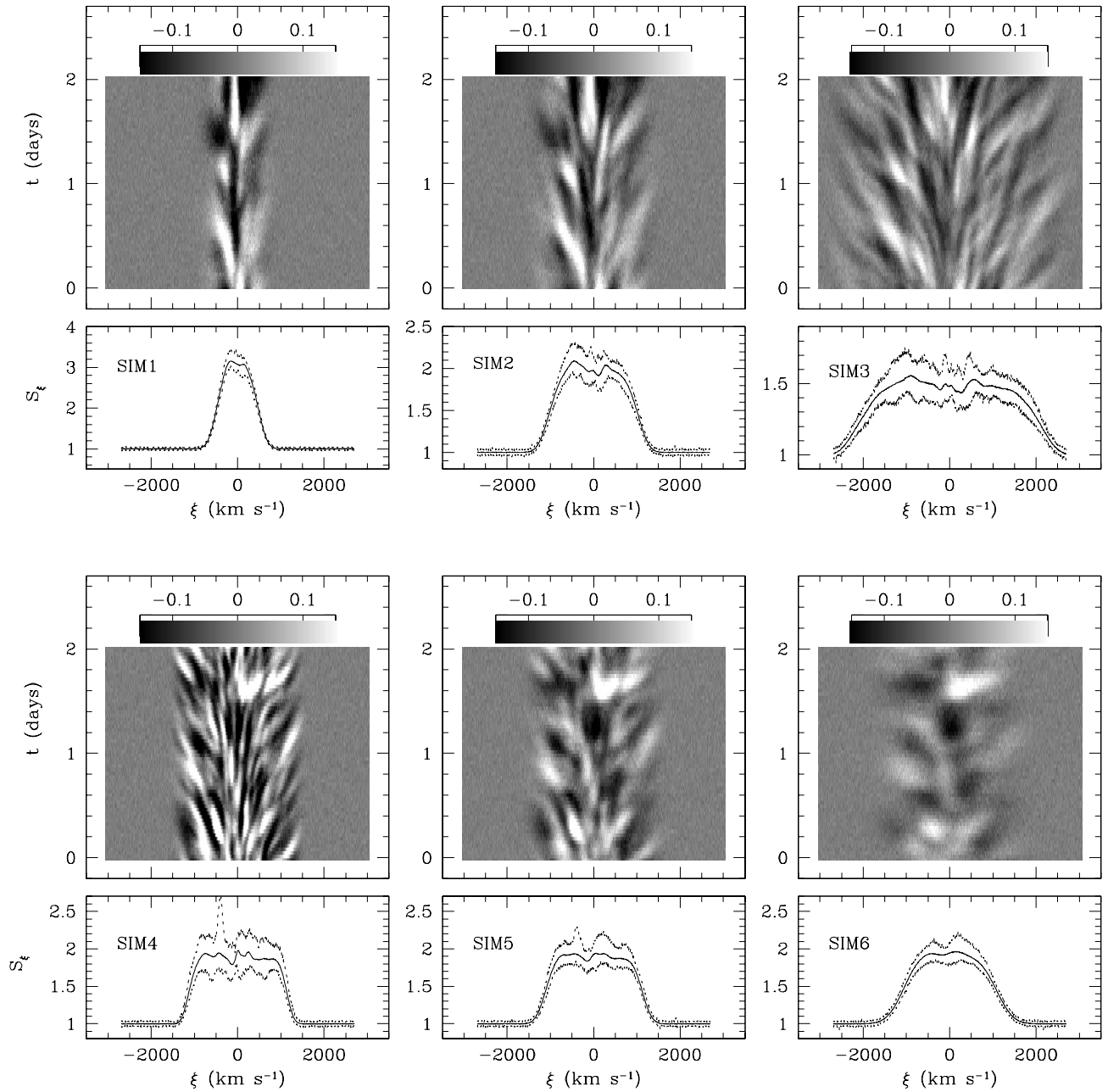


FIG. 7.—Simulations of LPVs from our model of radially propagating DWEs. The LPV pattern from one DWE distribution is shown to depend (*upper panels*) on the wind terminal velocity  $v_\infty$  and (*lower panels*) on the average width of emission subpeaks  $\sigma_\xi$ . Note how the number of apparent subpeak features is proportional to the ratio  $v_\infty/\sigma_\xi$ . Simulated spectral time series include 60 spectra spread over a 48 hr time base. The minimum, mean, and maximum line profiles are shown. Gray-scale plots show the residuals obtained after subtracting off the mean profile. The same DWE distribution was used in SIM 1, SIM 2, and SIM 3, and another one in SIM 4, SIM 5, and SIM 6. Model parameters are listed in Table 3.

Because  $\overline{\sigma_\xi}$  is approximately the same in all WR stars (see Fig. 4), the number of apparent subpeaks should be proportional to the line width, which in turn is proportional to  $v_\infty$ . We wish to emphasize that *the number of apparent subpeaks in LPV patterns is not related to the actual number of DWEs in the LER*; it simply reflects the spectroscopic resolving power for the emission line. Both  $v_e$  and  $\overline{\sigma_\xi}$  are intrinsic to the star. Therefore, one cannot hope to get higher  $R_w$  by instrumental means; there is a fundamental limit in the spectroscopic investigation of inhomogeneous wind structure. Since  $\overline{\sigma_\xi}$  is apparently independent of the stellar subtype, the best WR candidates for a study of the wind structure are those with the largest  $v_\infty$ .

If  $N_e$  is the mean number of DWEs in the emission-line region, the  $R_w$  spectroscopically resolved sectors consist of the emission from  $N_e R_w^{-1}$  wind elements. Let  $\overline{F_j}$  be the mean emission-line flux from the  $j$ th sector. The mean flux variation  $\sigma_{F_j}$  induced by the statistical variation in the number of DWEs in this sector will be

$$\sigma_{F_j} \propto \overline{F_j} N_e^{-1/2} R_w^{1/2}. \quad (20)$$

We can verify this relation by comparing the wavelet spectra for the simulations shown in Figure 7. In Figure 8, we present the normalized, mean wavelet power averaged over the emission-line region  $\langle \tilde{R}(\sigma_\xi) \rangle_{\text{LPV}}$ . These show that, for similar values of  $N_e$ , the magnitude of the variability in

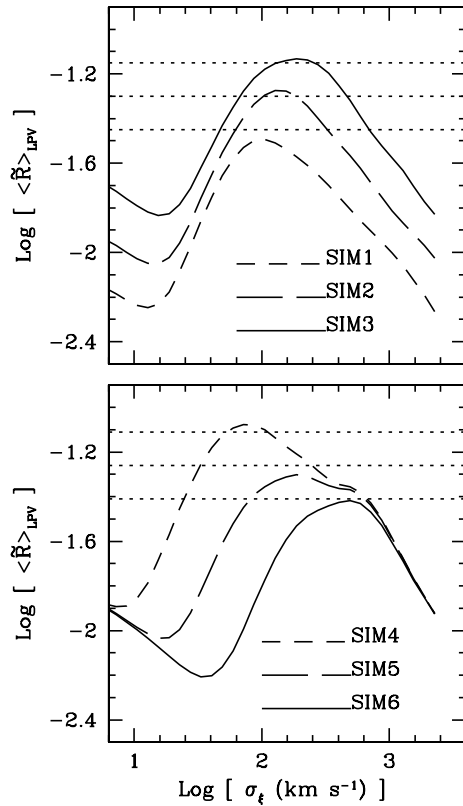


FIG. 8.—Wavelet power spectrum  $\langle \tilde{R}(\sigma_\xi) \rangle_{\text{LPV}}$  for the six simulations in Fig. 7. Dotted horizontal lines, spaced by  $1/2 \log 2$  intervals, show that the LPV amplitude is proportional to  $v_\infty^{1/2}$  and inversely proportional to  $\sigma_v^{1/2}$ . Note that the locations of the maxima in  $\langle \tilde{R}(\sigma_\xi) \rangle_{\text{LPV}}$  depend on the mean scale  $\sigma_\xi$  of LPV subpeaks.

the emission line is proportional to  $v_e^{1/2} \overline{\sigma_\xi}^{-1/2} = R_w^{1/2}$ , as predicted in equation (20).

#### 4.2. Statistical Distribution of DWEE Fluxes

Let an emission line with total line flux  $F_e$  be made up of a mean number  $N_e$  of DWEEs. If  $n(f)$  is the statistical distribution in flux of individual DWEEs, the standard deviation  $\sigma_{F_e}$  in the total line flux will be given by

$$\sigma_{F_e}^2 = \int_{f_0}^{\eta f_0} f^2 n(f) df. \quad (21)$$

Under the power-law distribution given in equation (13),  $\sigma_{F_e}$  has the general form

$$\sigma_{F_e} = F_e N_e^{-1/2} \sigma(\alpha, \eta). \quad (22)$$

We can calculate the function  $\sigma(\alpha, \eta)$  from equations (13), (14), and (15):

$$\sigma(\alpha, \eta) = \left( \frac{\eta^{1-\alpha} - 1}{1-\alpha} \right)^{1/2} \left( \frac{\eta^{2-\alpha} - 1}{2-\alpha} \right)^{-1} \left( \frac{\eta^{3-\alpha} - 1}{3-\alpha} \right)^{1/2},$$

$\alpha \neq 1, 2, 3;$

$$\sigma(1, \eta) = \sigma(3, \eta) = \left( \frac{\ln \eta}{2} \frac{\eta + 1}{\eta - 1} \right)^{1/2};$$

$$\sigma(2, \eta) = \left( \frac{\eta - 1}{\sqrt{\eta} \ln \eta} \right). \quad (23)$$

In the case in which all the DWEEs have approximately the same flux (e.g., if  $\eta \rightarrow 1$ ),  $\sigma(\alpha, \eta)$  converges to 1, and we get the familiar relation  $\sigma_{F_e} = F_e N_e^{-1/2}$ .

A plot of  $\sigma(\alpha, \eta)$  as a function of  $\alpha$  for different  $\eta$  is presented in Figure 9. One sees that significant deviations from the  $\sigma_{F_e} = F_e N_e^{-1/2}$  relation occur for small positive values of  $\alpha$  and for large  $\eta$ . Deviations occur when the statistical distribution is such that the total flux  $F_e$  is dominated by low-flux elements, while the fluctuations are mainly caused by high-flux elements making a small but nonnegligible contribution to  $F_e$ . Thus,  $\sigma(\alpha, \eta)$  converges to 1 for small values of  $\eta$  and for large values of  $\alpha$ , because these cases represent situations in which the number of high-flux elements is negligible.

For an emission line profile  $S(\xi)$  the standard deviation in the amplitude  $\sigma_S$  will be proportional to  $\sigma_{F_e}$  but will also depend on the spectroscopic wind resolution,

$$\sigma_S \propto \sigma(\alpha, \eta) N_e^{-1/2} R_w^{1/2}. \quad (24)$$

So far, we have used the normalized wavelet power spectrum  $\langle \tilde{R}(\sigma_\xi) \rangle_{\text{LPV}}$  to measure the amplitude in the LPVs. We used a large number of simulations to calibrate the relation between the maximum  $\langle \tilde{R}(\sigma_\xi) \rangle_{\text{LPV}}$  and  $\sigma_S$ , leading to

$$[\langle \tilde{R}(\sigma_\xi) \rangle_{\text{LPV}}]_{\text{max}} \simeq 0.3 \sigma(\alpha, \eta) N_e^{-1/2} R_w^{1/2}. \quad (25)$$

We present a synthesis of these results with simulations of LPV patterns from inhomogeneous winds obtained with various values of  $\alpha$ ,  $\eta$ , and  $N_e$ . Some of the resulting LPVs are shown in Figure 10. In Figure 11, we plot the wavelet power spectrum  $\langle \tilde{R}(\sigma_\xi) \rangle_{\text{LPV}}$ , obtained from each of the simulations. The maxima in the wavelet spectra are compared with the values predicted from equation (25), shown as dotted lines. The amplitudes of the maxima fall within  $\sim 10\%$  of the predicted values. However, except for the amplitude of the LPVs, the patterns look extremely similar. It is virtually impossible to guess which pattern comes from which simulation. This strongly suggests that *specific values*

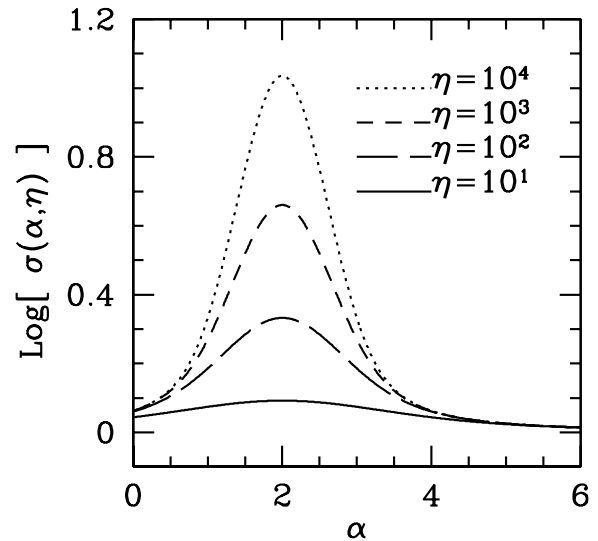


FIG. 9.—Variability induced by a distribution of DWEEs with a power-law distribution in their individual flux will depend on the power index  $\alpha$  and flux range  $\eta$ . This is demonstrated here with a plot of  $\sigma(\alpha, \eta)$  as a function of  $\alpha$ , for different values of  $\eta$ , where  $\sigma(\alpha, \eta)$  is a correction factor used in determining the total flux variability  $\sigma_{F_e}$  from a set of  $N_e$  individual DWEEs (see § 4.2).

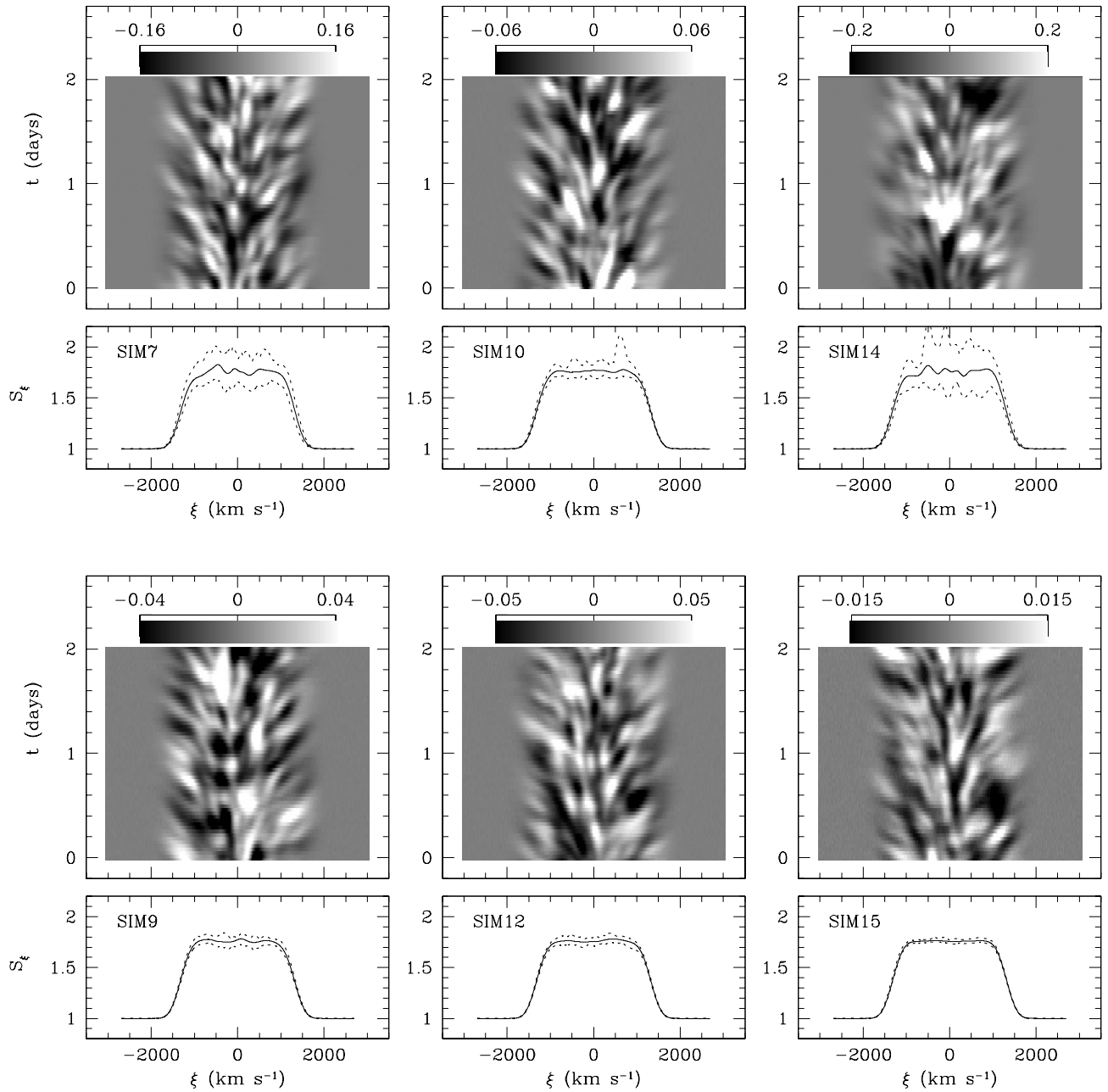


FIG. 10.—Simulations of LPVs, showing the dependence of the LPV patterns on the mean number  $N_e$ , power-law flux index  $\alpha$ , and flux range  $\eta$  of DWEs. Model parameters used in these simulations are listed in Table 3. The general patterns of the LPVs are indiscernible: unique determinations of  $N_e$ ,  $\alpha$ , and  $\eta$  cannot be obtained from such a spectral time series. Only the amplitude in the LPV varies, yielding constraints on a *combination* of these parameter values.

of  $\alpha$ ,  $\eta$ , and  $N_e$  cannot be estimated from the LPV patterns alone; only an estimate of  $\sigma(\alpha, \eta)N_e^{-1/2}$  can be obtained. This is a serious limitation to the study of inhomogeneous structure based on emission-line variability, although we may obtain constraints on possible ranges of values of  $\alpha$ ,  $\eta$ , and  $N_e$ .

We have used the wavelet power spectrum  $\langle \tilde{R}(\sigma_\xi) \rangle_{\text{LPV}}$  obtained from the data for our nine WR stars (see Fig. 4), combined with estimates of  $R_w$ , to evaluate  $N_e \sigma(\alpha, \eta)^{-2}$  for each star (see Table 4). They indicate that one would need at least  $10^3 \lesssim N_e \lesssim 10^4$  DWEs in the LER at any time to account for the LPVs in these WR stars. If there is a power-law distribution in the flux of individual DWEs such that  $\sigma(\alpha, \eta) > 1$ , several orders of magnitude more DWEs

might be required to account for the LPVs. We note that  $N_e$  represents only DWEs that lie in the LER, i.e., a relatively small fraction of the whole wind. We conclude that the structure of WR winds is probably extremely fragmented.

#### 4.3. Anisotropic Emission

We have run several simulations of line emission from inhomogeneous winds, with various values of the radial to angular velocity dispersion ratio  $\sigma_{v_r}/\sigma_{v_\theta}$  and of the radial to angular flux emission ratio  $f_r/f_\theta$ . Nine simulations were performed with combinations of  $\sigma_{v_r}/\sigma_{v_\theta} = [1, 2, 4]$  and  $f_r/f_\theta = [3.3, 1, 0.3]$ . White noise was added to simulate the presence of some instrumental noise. In Figure 12, we show the mean profiles obtained from a 48 hr spectral time series, along

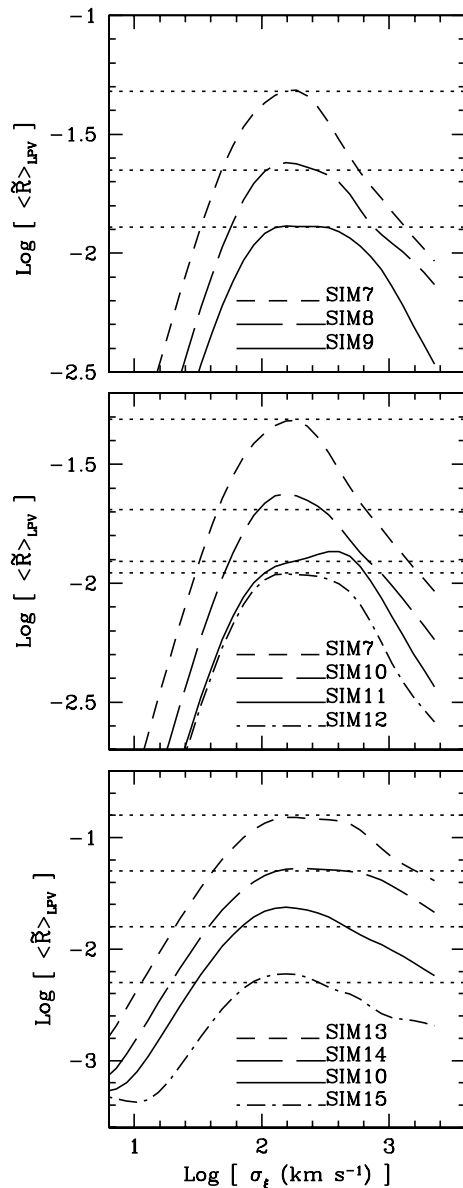


FIG. 11.—Wavelet power spectrum  $\langle \tilde{R}(\sigma_{\xi}) \rangle_{\text{LPV}}$  for the simulations SIM 7 to SIM 15, which were made using different numbers and flux distributions of DWEs (see Table 3). *Top panel*:  $\eta$  is varied while  $N_e$  and  $\alpha$  are fixed. *Center panel*:  $\alpha$  is varied, while  $\eta$  and  $N_e$  are fixed. *Bottom panel*:  $N_e$  is varied, while  $\alpha$  and  $\eta$  are fixed. Horizontal lines show the amplitude of the maxima in  $\langle \tilde{R}(\sigma_{\xi}) \rangle_{\text{LPV}}$  predicted from eq. (A2). All measurements fall within 10% of the predictions.

with the maximum and minimum spectrum profiles; the two-dimensional wavelet spectrum of the residuals is also plotted for each of the nine simulations.

The shape of the line profile is found to be strongly affected by the ratio  $f_r/f_\theta$ , but it seems almost unaffected by a reasonable degree of anisotropy in  $\sigma_v$ . The profile is especially sensitive to  $f_r/f_\theta > 1$ , where it yields something reminiscent of a profile generated by an emission ring. In the case in which  $f_r/f_\theta = 1$ , the profile is “flat topped,” whereas it looks somewhat rounded when  $f_r/f_\theta < 1$ . This works in the sense expected from optically thick line emission in a spherical, radial wind flow. Comparison with the observed mean profiles confirms that the shape of the C III  $\lambda 5696$  line is consistent with optically thin emission ( $f_r/f_\theta = 1$ ), whereas

the He II  $\lambda 5411$  line could be affected by optical-thickness effects.

The wavelet spectrum appears to be mainly sensitive to the ratio  $\sigma_v/\sigma_{v\theta}$ , but it is also affected by changes in the ratio  $f_r/f_\theta$ . One has to be careful in discriminating both effects. The ratio  $f_r/f_\theta$  affects the amplitude of the wavelet response as a function of  $\xi$ , whereas the ratio  $\sigma_v/\sigma_{v\theta}$  affects both the amplitude and the scale of the wavelet response. Statistical fluctuations also arise because of the limited sampling of the time series. The wavelet spectra from SIM 21 and SIM 24 are those that resemble most the wavelet spectra obtained from the data. Overall, we have found that the best fits are obtained with  $3 < \sigma_v/\sigma_{v\theta} < 5$ , and with  $f_r/f_\theta \lesssim 1$ .

The fact that we obtain  $f_r/f_\theta \lesssim 1$  from fitting the wavelet spectra of the LPV seems to be in contradiction with the impression that the C III line is optically thin. However, this could be explained if individual DWEs have different values of  $f_r/f_\theta$ . For example, high-flux DWEs may arise from wind elements with higher column density and might be more subject to opacity effects than low-flux DWEs. As mentioned in § 4.2, one can have a line whose global emission is dominated by the low-flux DWEs, while the LPV arises because of the high-flux DWEs. This would explain the observed effect on the wavelet spectra.

The addition of white noise in the simulations does not critically affect the wavelet response to the LPV. Since the noise varies on a pixel-to-pixel level, it consists only of very narrow features that show up in the Wavelet spectrum as a response near the smallest scale (in Fig. 12; this is the uniform response near  $\log [\sigma_{\xi}(\text{km s}^{-1})] \sim 1$ ). The noise is not a serious problem in our analysis because the spectral resolution is such that intrinsic features are at least several pixels in size. On the other hand, since the quality of the Wavelet spectrum depends on the size of the sample, larger spectral time series would improve the quality of the wavelet spectra, which could be used to investigate more subtle effects such as occultation of DWEs by the stellar disk.

#### 4.4. Kinematics of the Subpeaks

We have seen that variable subpeaks tend to persist on emission line profiles for a certain period of time and that subpeak features show a systematic motion from the line center to the line edges. This behavior is suggestive of radial expansion of wind features. The general evolution in time of the LPV pattern depends on the wind dynamics and line-emission structure. The simplest interpretation for the characteristic timescale of a subpeak event relates it to the time it takes for the wind feature to cross the LER, whereas subpeak motion reflects the wind acceleration in the LER.

In order to keep the analysis as objective as possible (i.e., without having to rely on the identification of “individual” subpeak events), we introduce the “degradation function” as an analysis tool. The degradation function, denoted  $\sigma_D(a, \Delta t)$  (see Appendix B) is similar to a correlation function and is used to estimate the mean radial acceleration  $a_e$  of DWEs in the LER and the velocity range  $\sigma_{v_e}$  of this LER from the LPV pattern. The quality of  $\sigma_D(a, \Delta t)$  is proportional to the size of the data sample, which must include pairs of spectra with temporal separations shorter than the subpeak lifetimes. This requirement is necessary to obtain a reliable estimate for  $a_e$ .

The minimal degradation value of  $\sigma_D(a, \Delta t)$  is obtained when parameter  $a$  is set to  $a = a_e$ . More reliable estimates



TABLE 4  
WIND PROPERTIES FROM THE LPV PATTERNS

WR Number	$\overline{\sigma}_\xi$ (km s <sup>-1</sup> )	$N_e \sigma(\alpha, \eta)^{-2}$	$a_e$ (m s <sup>-2</sup> )	$\sigma_{v_e}$ (km s <sup>-1</sup> )	$\sigma_{v_r}$ (km s <sup>-1</sup> )
WR 40 .....	90 ± 20	1.6 ± 0.6 × 10 <sup>3</sup>	3.5 ± 1.5	60 ± 15	115 ± 18
WR 103 .....	120 ± 25	3.5 ± 1.4 × 10 <sup>3</sup>	4.5 ± 1.5	70 ± 15	210 ± 22
WR 111 .....	90 ± 20	1.5 ± 0.6 × 10 <sup>4</sup>	20.0 ± 5.0	120 ± 20	135 ± 22
WR 134 .....	350 ± 75	2.0 ± 0.8 × 10 <sup>3</sup>	25.0 ± 3.0	285 ± 40	145 ± 49
WR 135 .....	120 ± 25	9.5 ± 3.8 × 10 <sup>3</sup>	11.0 ± 1.5	100 ± 25	140 ± 27
WR 136 .....	90 ± 20	4.1 ± 1.7 × 10 <sup>4</sup>	5.5 ± 1.0	80 ± 20	280 ± 25
WR 137 .....	75 ± 15	2.4 ± 1.0 × 10 <sup>4</sup>	8.5 ± 3.5	95 ± 20	165 ± 22
WR 138 .....	110 ± 25	6.9 ± 2.7 × 10 <sup>3</sup>	9.0 ± 1.5	135 ± 30	215 ± 34
WR 140 .....	90 ± 20	3.6 ± 1.4 × 10 <sup>4</sup>	12.0 ± 2.5	90 ± 25	175 ± 27

NOTES.—All values are estimated from the LPV patterns:  $\overline{\sigma}_\xi$  is the average width of subpeak features,  $N_e$  is the mean number of DWEEs in the LER (see § 4.2),  $a_e$  is the radial acceleration of DWEEs,  $\sigma_{v_e}$  is the estimated size of the LER for one DWEE. The values listed for  $\sigma_{v_r}$  are the radial velocity dispersions needed to account for the large  $\Delta v_e$  (see Table 2) provided that  $\sigma_{v_e}$  are reliable measures for the size of the LER.

can be obtained from  $\langle \sigma_D(a) \rangle_{\Delta t < t_e}$ , i.e., the mean degradation obtained from all pairs of spectra separated by  $\Delta t < t_e$ , where  $t_e$  is shorter than the estimated duration of subpeak events. We present in Figure 13 the mean degradation  $\langle \sigma_D(a) \rangle$ , estimated from pairs of spectra separated by  $\Delta t < 3$  hr, for each of the WR stars in our data set. The locations of the minima yield estimates of  $a_e$ , which are listed in Table 4; they range from  $\sim 3.5$  m s<sup>-2</sup> in WR 40 to  $\sim 25$  m s<sup>-2</sup> in WR 134. To facilitate the comparison between the stars, we have plotted in Figure 13 the normalized  $\langle \sigma_D(a) \rangle / \langle \sigma_D(a_e) \rangle$ .

We summarize the results in Figure 14, where we plot the nondimensional stellar wind acceleration  $a_e R_\odot v_\infty^{-2}$  as a function of the normalized wind velocity  $v_e v_\infty^{-1}$ . This plot indicates the relative wind acceleration as a function of wind depth, where we use the relative radial wind velocity  $v_e v_\infty^{-1}$  as a depth measure. We compare the measurements from the stars to the values expected from idealized  $\beta$ -type wind velocity laws having different values of the parameter  $\beta R_*$  (see § 3.2). The estimates all correspond to  $\beta$ -laws with  $20 < \beta R_* R_\odot^{-1} < 80$ .

The duration of subpeak events can be estimated from a plot of  $\sigma_D(a_e, \Delta t)$  (e.g., Fig. 15). One sees in Figure 15 that  $\sigma_D(a_e, \Delta t)$  increases steadily with  $\Delta t$  until it asymptotically reaches some constant level. From that moment onward, any correlation is lost, which indicates that the time interval has become larger than the subpeak duration. All structures initially present in the signal have disappeared, which explains the loss of correlation.

Using the estimated values of  $\beta R_*$  obtained from the accelerations  $a_e$ , we performed simulations of LPVs using the model described in § 3. For each star in our data set, we performed independent simulations using the same time base and selecting values of  $a_e$  to match those obtained from Figure 13. For each star, the degradation function  $\sigma_D(a_e, \Delta t)$  from the data was compared to that obtained from the matching simulation; the results are shown in Figure 15. We performed the simulations by first trying  $\sigma_{v_e} = \Delta v_e$  (i.e., neglecting the turbulent broadening  $\sigma_\xi$ ; see eq. [11]), as the extension of the LER expressed in wind velocity space (*short-dashed line*). This attempt resulted in poor agreement with the data, the longer lifetime of the subpeak features revealing that the size of the LER had been overestimated. Better fits were obtained with smaller

values for  $\sigma_{v_e}$  (*long-dashed lines*), which are listed in Table 4. From these, we evaluated the radial wind velocity dispersion  $\sigma_{v_r}$ , which would account for the dispersion  $\Delta v_e$  in the emission-line profile (see eq. [11]).

For most of the stars, the estimated  $\sigma_{v_r}$  are consistent with what has been suggested from the wavelet analysis, namely that  $\sigma_{v_r} \sim 4\sigma_{v\theta}$ . Wavelet analysis of simulations made with these values typically yield  $\overline{\sigma}_\xi \approx \sigma_{v_r}/2$ . The star WR 134 again makes the exception, having  $\sigma_{v_r} < \overline{\sigma}_\xi$  instead. One also sees that  $\sigma_{v_e}$  is apparently much larger for this star, although the emission line profile is not very different from that in other WR stars. This is further evidence that the LPVs in WR 134 cannot be accounted for by radially propagating wind features. The large, apparent  $\sigma_{v_e}$  would be consistent with a wind structure having a motion in  $\hat{\theta}$  as well as in  $\hat{r}$ . For the other WN stars, because of the possible optical depth effects, we suspected that  $\Delta v_e$  would overestimate the actual dispersion in the line emission (see § 3.3). One sees that this might indeed be the case for some of the WN stars: e.g., for WR 136, we find  $\sigma_{v_r} \sim 3\overline{\sigma}_\xi$ , which can be reproduced with a ratio  $\sigma_{v_r}/\sigma_{v\theta} \sim 9$ , much larger than what is inferred from the wavelet spectrum.

The flat-topped C III line in the WC stars stands out as the line that is best suited for a comparison with our simulations. We note that the size of the LER contributes only a minor part of the emission-line broadening  $\Delta v_e$ . It is the “turbulent” motions, as revealed by the width of variable subpeaks, which dominate the line broadening. It appears that the size of the LER would be relatively small, at least for the C III transition.

## 5. DISCUSSION

### 5.1. Physical Origin for the Variable Emission Elements

Our analysis of the LPVs in WR emission lines strongly suggests that a very similar phenomenon is at work in all the stars, independent of the spectral sequence and subclass. Except for the peculiar (and periodic) case of HD 191765, the LPVs can be reproduced using the same model of radially propagating, stochastic inhomogeneities. The fact that the physical aspect of the subpeaks, i.e., their velocity dispersion, does not depend on the geometry of the LER, the magnitude and acceleration of the wind velocity, or the depth in the wind at which the line is formed, is suggestive

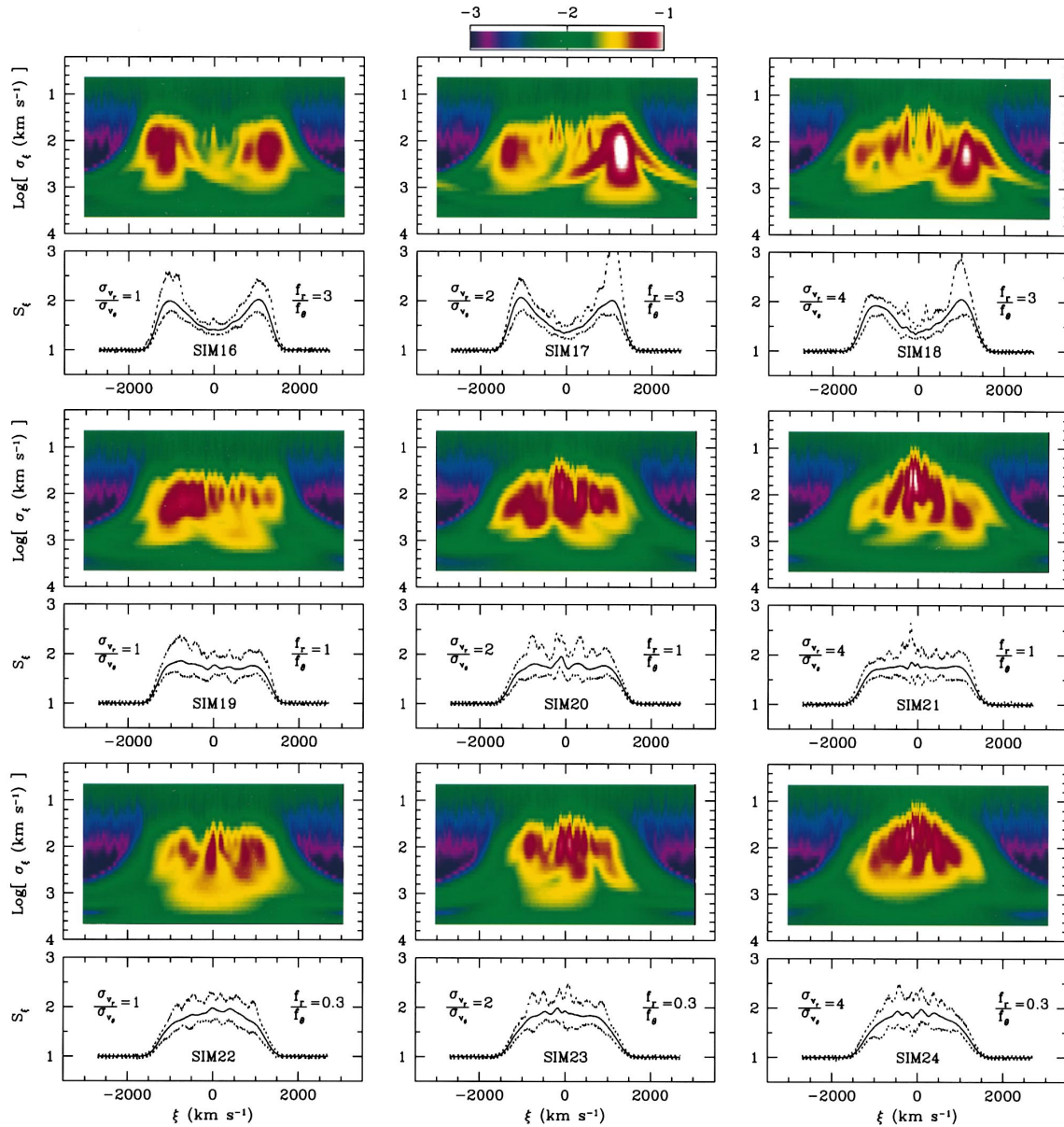


FIG. 12.—Simulated LPV showing the effects of anisotropic velocity dispersions and photon escape probabilities. The parameters of the simulation are listed in Table 3. The minimum, mean, and maximum profiles from 48 hr long spectral time series are shown. The shape of the mean profile is sensitive to the emissivity ratio  $f_r/f_\theta$ , especially when  $f_r/f_\theta > 1$ . The mean wavelet spectrum of the spectral time series (*top panels*) is sensitive to the ratio  $\sigma_{v_x}/\sigma_{v_y}$ . A comparison with Figs. 1, 2, and 3 suggests that inhomogeneous features in WR winds have  $\sigma_{v_x}/\sigma_{v_y} \simeq 4$ . We can rule out the possibility that  $f_r/f_\theta > 1$  in WR stars, because of the shape of WR emission-line profiles. The LPV patterns seem to be consistent with  $f_r/f_\theta \lesssim 1$ , though the flat-topped C III profiles seem to argue against this possibility (see § 4.3).

of some universal process within the inhomogeneous WR wind structure.

One conclusion to be drawn is that variable subpeaks must reflect strong, local velocity gradients. One cannot explain easily the large  $\sigma_v$  in terms of the extension in space of an overdense region, for which the velocity dispersion would simply reflect the range in radial bulk wind velocity within the region. One reason is that one would then expect to observe different  $\sigma_v$  in different stars, depending on the wind velocities and accelerations. Another reason is that the very large number ( $\gg 10^3$ ) of wind elements that are required to model the LPVs suggests that individual DWEs occupy relatively small volumes. The large velocity dispersions are more easily explained in terms of large local random motions such as from macroturbulence, or large

local systematic motions such as from shocks in large-scale stream interactions (see Cranmer & Owocki 1996).

We believe that the observed  $\sigma_{v_x}/\sigma_{v_y} \sim 4$  reflects a true anisotropy in the velocity dispersion. The large ratio might be reproducible from radiative transfer effects in optically thick wind clumps, but such effects would likely show up in the shape of the emission-line profile as well, in the form of deviations from a flat-topped profile. Since we do not see any such large deviations, at least for the C III  $\lambda 5696$  line in the WC sequence, the only possibility would be that only some DWEs (likely in the high-flux regime) would show these optical depth effects. However, in this case, we should also detect narrow (although weaker) subpeaks near the edges of the line; this is apparently not the case. Thus, although we believe that optical depth effects might be

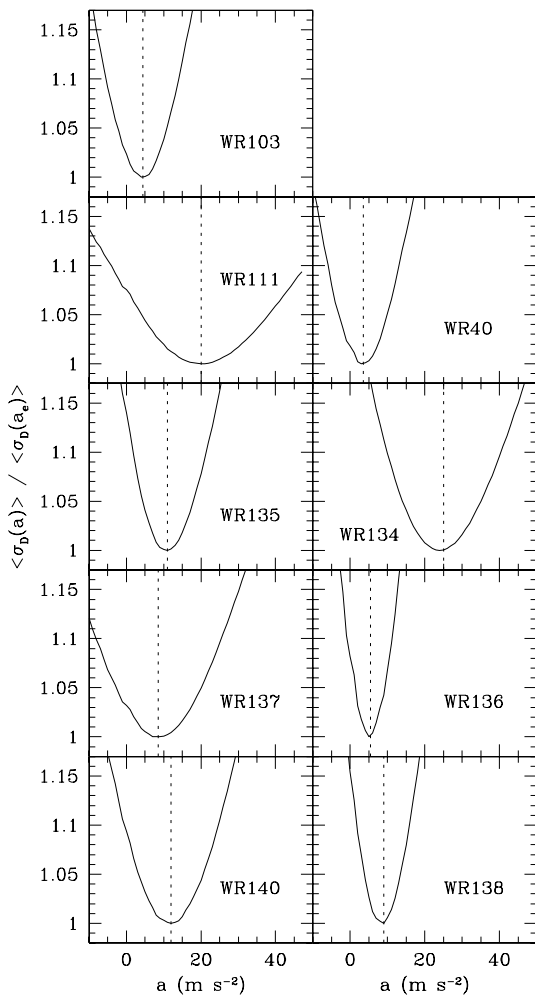


FIG. 13.—Radial acceleration  $a_e$  of wind inhomogeneities, as obtained from the mean degradation function  $\langle \sigma_b(a) \rangle$  of LPV patterns, from pairs of spectra separated by  $\Delta t < 3$  hr. The minima yield estimates of the radial wind acceleration  $a_e$  in the LER (see Appendix B). We obtain estimates in the range  $4 < a_e < 25 \text{ m s}^{-2}$  (see Table 4).

affecting some DWEs, yielding  $f_r/f_\theta \lesssim 1$ , the  $\sigma_{v_r}/\sigma_{v_\theta}$  ratio most likely depends on the real velocity dispersion within DWEs.

Anisotropic turbulence is believed to exist in the chromospheres of some stars (see, e.g., Carpenter & Robinson 1997). However, the latter imply motions of  $\sigma_v \sim 20\text{--}30 \text{ km s}^{-1}$ , substantially lower than what we measure (we note that our observed  $\sigma_v$  correspond to highly supersonic motions). It is not clear how coherent wind features with such large internal random motions can persist for long enough to be observed as discrete wind features. Should hydrodynamical viscous dissipation occur, a hierarchy of clumps will also be expected to form, governed by specific scaling laws (Henriksen 1991). This means that smaller clumps, i.e., shocks having smaller velocity dispersions, should be present in the wind. This makes the analysis of the variable subpeak patterns still more complex, since our assumption that all clumps have the same velocity dispersion would be only approximate. This specific problem of scaling relations in the clumps was investigated in Paper I, in which we presented marginal observational support for the existence of such scaling laws and obtained constraints on the possible scaling properties. One consequence of

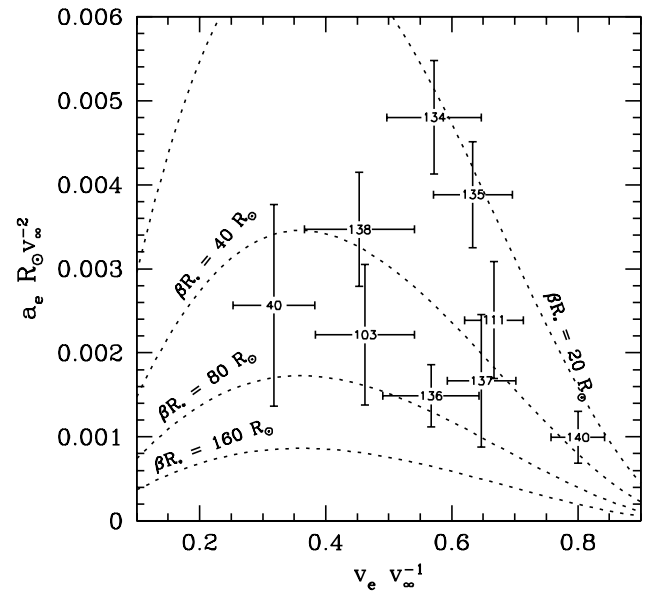


FIG. 14.—Comparison between the dimensionless acceleration  $a_e R_\odot v_\infty^{-2}$  and the relative velocity range  $v_e v_\infty^{-1}$  in the wind, as estimated from the LPVs in the WR stars of our sample. Dashed lines show the ratios expected from  $\beta$ -laws for various values of the combined  $\beta R_*$  parameter. The kinematics of the WR LPV subpeaks are consistent with  $20 < \beta R_* R_\odot^{-1} < 80$ , much larger than the values typically used in theoretical WR wind models. The large dispersion in  $\beta R_*$  for the stars in the sample might reflect either different values in their core radii or simply indicate the inadequacy of one general  $\beta$ -law as a good representation of WR wind velocity fields.

supersonic turbulence, or self-structured chaos (see Henriksen 1994), is that coherent wind features could survive for only a limited time, possibly yielding a subpeak timescale that is shorter than expected from the crossing time through the LER.

The supersonic/anisotropic behavior could also be accounted for by the existence of radially propagating shocks. It has been shown that the radiation line-driving mechanism is unstable and that strong shocks can form and propagate in a radiatively driven wind (Owocki, Castor, & Rybicki 1988). These shocks are usually thought to be initiated by hydrodynamical perturbations at the base of the wind, such as stellar pulsations or surface inhomogeneities in conjunction with stellar rotation (Owocki, Cranmer, & Fullerton 1995). These mechanisms may account for the periodic wind fluctuations such as in the discrete absorption component (DAC) phenomenon in OB stars (Cranmer & Owocki 1996) but could be hard to reconcile with the stochastic behavior of the WR LPVs. However, it has been shown that the growth rates of instabilities in WR winds are likely to be extremely large, such that small, random fluctuations could grow into the stochastic shocks that we observe (Gayley & Owocki 1995).

However, it has been claimed that shock propagation in winds driven by line scattering should be “polarized” in the radial direction (Rybicki, Owocki, & Castor 1990), i.e., damped in other directions. Our results provide direct evidence supporting this claim. We note, however, that even though wind perturbations are such that  $\sigma_{v_\theta} \ll \sigma_{v_r}$ , we might still get relatively large apparent measures of  $\sigma_{v_\theta}$  because of the finite angular extension of the perturbation. For example, a radially propagating shock with angular size  $\Delta\Omega \simeq 0.2 \text{ sr}$  and radial velocity dispersion  $\sigma_{v_r}$  would yield

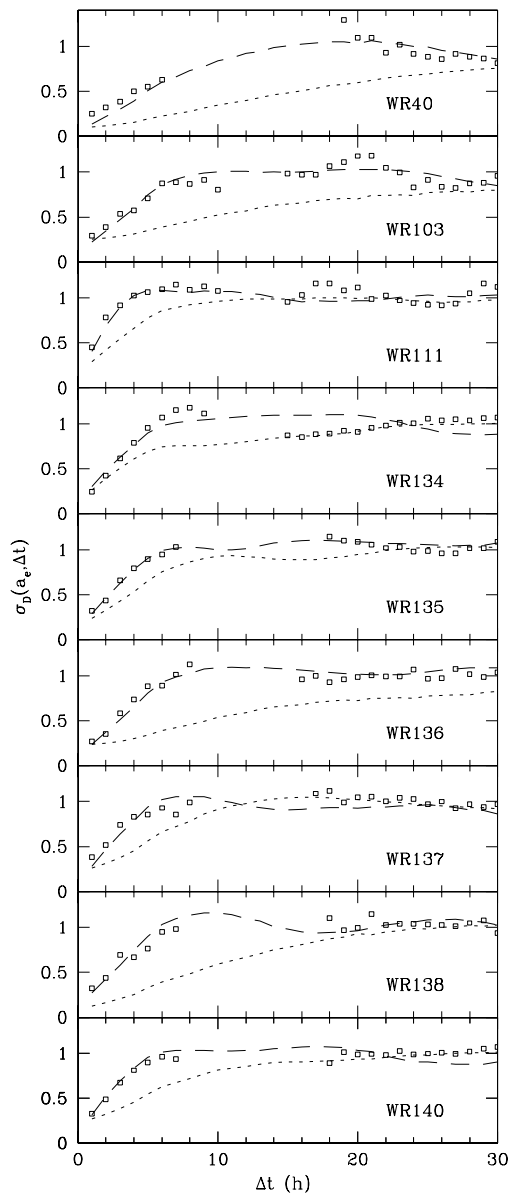


FIG. 15.—Comparison between the degradation function  $\sigma_D(a_e, \Delta t)$  obtained from the data (squares) with that from simulated LPVs. For each star, we present one simulation that uses  $\Delta v_e$  as the full range  $\sigma_{v_e}$  of the LER (dotted lines), i.e., that assumes that there is no turbulent broadening in the profile and that  $\Delta v_e$  yields a correct estimate of the DWEs velocity range (see § 3.3). The  $\sigma_D(a_e, \Delta t)$  for these simulations are found to disagree with the data. A better fit was obtained using much smaller depths for the LER (dashed lines). These smaller values suggest a radial turbulent broadening  $\sigma_{v_r} \sim 2\sigma_{v_e}$ . This is consistent with the results obtained from the wavelet analysis that suggested anisotropic velocity dispersion (see § 4.3).

an apparent  $\sigma_{v_\theta} \simeq \sigma_{v_r}/4$  when observed to propagate perpendicular to the main propagation axis. Such large angular sizes (about 1/50 of a spherical shell) could be reconciled with a large  $N_e$ , since shocks could be relatively shallow in the radial direction. It is not clear, however, why shocks would then tend to have similar angular sizes.

## 5.2. The Wind Velocity Structure

The wind acceleration is a crucial quantity for testing the velocity law. This test is critical because the velocity law is

usually assumed in modeling the winds and atmospheres of WR stars (see Hillier 1996). The degradation function provides reliable estimates of  $a_e$ , the radial acceleration of DWEs. However,  $a_e$  might not be equal to the radial acceleration of the wind material: if DWEs arise, e.g., from shock compressions, the corresponding density enhancements (compressions patterns) might be moving *relative to the mean motion* of wind material. The question is whether this motion relative to the bulk wind velocity would bias the  $a_e$  measures. If we believe this effect to be unimportant (or nonexistent), there is still a basic uncertainty in the determination of the velocity law from emission subpeaks. Spectroscopy provides only information in velocity space, and because the magnitude of the acceleration depends linearly on the product  $\beta R_*$ , it is not possible to evaluate  $\beta$  or  $R_*$  separately.

Nevertheless, our estimates of  $\beta R_*$  may provide interesting constraints on the  $\beta$ -law in WR winds. So far, we obtain  $\beta R_*$  values that are not consistent with the values commonly used in WR wind models. For instance, values of  $\beta = 1$  and a core radius  $R_* = 3 R_\odot$  have been used to model the wind from WR 111 (Hillier 1989), whereas we find  $\beta R_* \sim 30$  for this same star. Non-LTE spectral analysis of the WN star WR 136 yielded  $R_* = 6.4 R_\odot$  with  $\beta = 1$  (Hamann et al. 1994), whereas we find  $\beta R_* \simeq 70$ . These results were obtained from using the “standard model” hypotheses, including homogeneity. More recently, Schmutz (1997) has performed a spectral analysis of HD 50896, this time using a clumped wind model. He obtained a velocity law that was fitted (in the outer wind regions) with  $\beta = 8$ ,  $R_* = 3.5 R_\odot$ . This appears to be in better agreement with our analysis, though a study of the LPVs in HD 50896 would be required to confront this result. Still, the  $\beta R_*$  that we measure in some stars is significantly larger than what is obtained from most models.

The source of this discrepancy might reside in the fact that the parameter  $R_*$  in the  $\beta$ -law is not related to the stellar core radius. Close binary systems provide upper limits for the core radii of the components, since the size of the orbit must always be larger than the sum of the radii of the component stars. There exist a few WR stars in very short period WR+O binaries, such as CQ Cep with a period of 1.6 days. Upper limits to the core radii of six WN stars (including CQ Cep) in close binary systems have been estimated to be in the range 2–10  $R_\odot$  (Moffat & Marchenko 1996). It is not clear whether the results from binary stars should apply to our sample of single WR stars, since single WR stars may have evolved differently from WR stars in binary systems (Dalton et al. 1995; see however Moffat 1995). Therefore, either we adopt large values for  $\beta$  or we abandon the idea that  $R_*$  is related to the core radius. Using values of  $R_*$  that are larger than the core radius will result in a failure for the  $\beta$ -law to describe the velocity field close to the stellar radius.

In any case, we can still attempt to fit the velocity structure at larger  $v$  with a  $\beta$ -law. Depending on the actual velocity structure near  $v = 0$ , we will obtain  $R_*$  values that can be either larger or smaller than the core radius. The analysis of HD 50896 by Schmutz (1997) appears to be consistent with this view and suggests that there is a divergence from the  $\beta$ -law form at small distances from the stellar surface. On the other hand, models of radiation-driven winds (see, e.g., Gayley, Owocki, & Cranmer 1995; Springmann 1994) suggest a more extended wind-acceleration region than that

from the  $\beta$ -law, which could actually result in a smaller than expected acceleration near to the star for a given terminal velocity.

There remains the possibility that the apparent motion of DWEs in velocity space does not reflect the actual mean hydrodynamical wind flow. If the inhomogeneous structure is in the form of radially propagating shocks, and if we rely on the smaller, theoretical estimates of  $\beta R_*$ , this implies that shocks have smaller radial acceleration than the wind material. This might be explained with shocks propagating toward the star, in the wind rest frame, like the “reverse shocks” found by Owocki et al. (1988) in one-dimensional simulations of radiatively driven winds. In this hydrodynamical model, it was found that shocks of different sizes seemed to propagate at different rates, denser shocks having a lower radial acceleration. Such a behavior might eventually be verified, by testing whether the LPV subpeaks are consistent with intense DWEs having low acceleration (high  $\beta R_*$ ), and weaker DWEs having higher accelerations (low  $\beta R_*$ ).

### 5.3. The Size of the LER

We have interpreted the timescale of LPV subpeaks as the crossing of one DWE through the LER. Using our estimates for the radial acceleration of DWEs, we have estimated the size in velocity space  $\sigma_{v_e}$  of the LERs for the WR stars in our sample. We have found relatively small values, which suggest that  $\sigma_{v_e}$  is not the main factor responsible for the emission-line broadening  $\Delta v_e$ .

The large  $\Delta v_e$ , estimated from the shape of the emission-line profiles (see § 3.3), can be accounted for by the large radial velocity dispersion  $\sigma_{v_r}$  within the DWEs, provided that  $\sigma_{v_r} \sim 2\sigma_\xi$ , where  $\sigma_\xi$  is the mean velocity dispersion measured from the LPV subpeaks. This is consistent with the conclusions from the wavelet analysis, which suggest large anisotropies in the velocity dispersion, with  $\sigma_{v_r} \sim 4\sigma_{v_\theta}$ .

A small  $\sigma_{v_e}$ , however, does more than just corroborate the anisotropic velocity dispersion hypothesis; it also supports the view that the whole line emission comes from DWEs having large  $\sigma_{v_r}$ . We have assumed in our model that the whole line arose from DWEs and that the velocity dispersion vector  $\sigma_v$  (see § 3.4) was the same for all DWEs. However, the LPV patterns could not provide any support to this view, because one cannot know whether the LPV subpeaks reflect the physical properties of all DWEs, or only a few, especially large ones.

For example, in the case where there is a power-law distribution in the DWE fluxes, most of the line emission  $F_e$  might arise from the low-flux DWEs, while the variability  $\sigma_{F_e}$  is dominated by the high-flux components. In Paper I, we have investigated the possibility that there could be a proportionality relation between the flux and the velocity dispersion of DWEs. If this were the case, then the large  $\sigma_\xi$  might reflect only the velocity dispersion of the high-flux DWEs. However, the small values of  $\sigma_{v_e}$  indicate that large  $\sigma_{v_r}$  must prevail for the whole wind emission.

One could blame the small  $\sigma_{v_e}$  on a systematic bias in the degradation function, such as effects of standing but variable features (e.g., atmospheric lines, noise). These might bias the measure of the acceleration to smaller values, in turn leading to underestimates in  $\sigma_{v_e}$ . The degradation in the signal might also be “accelerated” by the noise, which might induce underestimates in the characteristic time duration. However, we verified the effect of synthetic noise

on the simulations and did not find significant deviations in the measure of  $\sigma_{v_e}$ .

On the other hand, there are physical effects that would yield an underestimate of  $\sigma_{v_e}$  from the degradation function. These would be responsible for the short timescale of variable subpeaks while accounting for the large  $\Delta v_e$  in the line profile without having to rely on the existence of large local turbulent motions: (1) a large random motion of DWEs relative to one another, (2) variable locations of the LER for individual DWEs, and (3) rapid fluctuations in the density structure.

The width of one LPV subpeak depends on the velocity dispersion within the region occupied by the corresponding DWEs. Large random motions could exist that would not be reflected in the width of LPV subpeaks, e.g., the motion of one clump relative to others. These “macroturbulent” motions would affect the shape of the emission line profile, increasing the  $\Delta v_e$ , but would not be detectable from the LPV pattern.

We have assumed so far that each and every DWE has the same emissivity function, i.e., that the location of the LER was an independent quantity. However, the emissivity of one DWE as a function of wind depth might depend on its density. Since DWEs represent stochastic wind fluctuations, it is reasonable to assume that inhomogeneous components will not all be emitting from the same wind region. While individual subpeaks could emit only within a narrow region from the star, they could, as a whole, be emitting from a much larger region.

Finally, the inhomogeneous wind structure might be rapidly fluctuating, as in models of self-structured chaos, or turbulent energy dissipation. The relative density of DWEs may also be changing because of pressure gradients. It is therefore possible that our  $\sigma_{v_e}$  would not measure the crossing time of one DWE through the LER, but rather measure the lifetime of inhomogeneous wind features. The actual size of the LER could therefore be larger, although we may still account for the small  $\sigma_{v_e}$  measured from the degradation function method.

## 6. SUMMARY AND PERSPECTIVES

We have presented a set of high-resolution spectra for nine WR stars. The spectra show time series of the C III  $\lambda 5696$  emission line for five stars of the WC sequence and the He II  $\lambda 5412$  emission line for four stars of the WN sequence. The time series each cover 3–4 consecutive nights, with spectral sampling every hour or so. The time series reveal the presence of line profile variations (LPVs) on the order of 5% of the line intensity. The LPVs show characteristic patterns, with narrow emission subpeaks moving from line center toward line edges on both halves of the line. The universality of the phenomenon is supported by recent detection of similar LPVs in an O-star wind (Eversberg, Lépine, & Moffat 1998).

We have investigated the hypothesis that these LPVs could be due to radially propagating wind inhomogeneities. We developed a simple phenomenological model that uses a random distribution of discrete wind emission elements (DWEs). These DWEs are assumed to propagate radially according to some monotonically increasing velocity law  $v(r)$  and to be emitting line radiation as they cross a corresponding line-emission region (LER), which has the form of a spherical shell with some arbitrary thickness. We used the so-called  $\beta$ -law in the form  $v(r) = v_\infty(1 - R_* r^{-1})^\beta$ ,

with  $v_\infty$  the terminal wind velocity. Both the location of individual DWEEs and the location/thickness of the LER are expressed in wind velocity space. The DWEEs are assigned a certain velocity dispersion, which represents the local deviations from the wind velocity law, such as turbulent motions or shocks. The model also allows for some optical depth effects within individual DWEEs, although these are assumed to be optically thin to one another.

We used this model to generate time series of synthetic emission-line spectra, which were shown to reproduce well the observed LPV patterns. Synthetic spectra were used to investigate how model parameters affect the shape of the emission-line profile and the pattern of LPVs. We found that a finely structured inhomogeneous wind, requiring a huge number of DWEEs, could yield LPV patterns in which only a few apparent subpeak events are observed. The actual number of subpeak events detected at any time was shown to depend on  $R_w \equiv v_e \bar{\sigma}_\xi^{-1}$ , the ratio of the wind velocity  $v_e$  (related to the emission-line width) to the mean line-of-sight velocity dispersion  $\bar{\sigma}_\xi$  of variable subpeaks.

We used the continuous wavelet transform as a multi-scale analysis tool for the study of LPV patterns. This numerical tool is shown to be very useful in many ways, in that it can also be used to distinguish intrinsic, variable features in the signal (large-scale response) from instrumental noise variability (small-scale response). We found intrinsic features with mean velocity dispersions  $\bar{\sigma}_\xi \sim 100 \text{ km s}^{-1}$ , with only one exception (HD 191765, where  $\bar{\sigma}_\xi \simeq 350 \text{ km s}^{-1}$ ). Wavelet analysis showed that LPV subpeaks are narrower near the line center than near the edges, i.e., that the velocity dispersion is larger for DWEEs that are propagating along the line of sight. This suggests that the velocity dispersion of DWEEs is larger in the radial direction than in the azimuthal direction, with  $\sigma_{v_r} \sim 4\sigma_{v_\theta}$ . Wavelet analysis also provided marginal evidence for optical depth effects, with an escape probability within DWEEs possibly smaller in the radial direction. However, the flat-topped shape of the C III  $\lambda 5696$  line in stars of the WC sequence suggests that only some of the DWEEs might be affected by optical thickness effects.

Systematic temporal variations in the LPV patterns were investigated with the use of the so-called degradation function, which finds correlations between different spectra in the time series. The degradation function is used to determine the magnitude of the radial acceleration of DWEEs and the characteristic duration of the subpeak events. These sources of information are used to investigate both the velocity law (from the acceleration) and the size in velocity space of the LER (relating it to the duration of subpeak

events). Data analysis revealed smaller accelerations than expected. We found that the data could be fit with a  $\beta$ -law with  $20 < \beta R_* R_\odot^{-1} < 80$ , an order of magnitude larger than predicted by homogeneous models of WR winds.

We compared the data to simulations, to determine the size of the LER that best reproduced the duration of subpeak events. These fits resulted in relatively small sizes for the LER, much smaller than the observed line-profile broadening  $\Delta v_e$ . This suggests that most of the line broadening arises from a large, “turbulent” radial velocity dispersion, which must be  $\sigma_{v_r} \sim 2\bar{\sigma}_\xi$ . Simulations show this result to be consistent with large anisotropic velocity dispersion with  $\sigma_{v_r} \simeq 4\sigma_{v_\theta}$ . This result thus yields independent evidence for anisotropy, while suggesting that  $\sigma_{v_r}$  must be affecting the whole line emission and not just a few intense DWEEs. Other possible interpretations were also discussed (§ 5.3).

One of the stars (HD 191765) is shown to yield results that are inconsistent with our model of radially propagating wind features. The large-scale, LPV pattern from this star was already known to be somehow peculiar, being recurrent rather than stochastic, as in other WR stars. A better model for this peculiar star might involve the rotation of a structured wind (Morel et al. 1997, 1999).

Overall, this new method for the analysis of LPV patterns has yielded several new constraints on the inhomogeneous and dynamical structure of WR winds. Since our numerical tools use statistical measures that combine the information from several consecutive spectra, we expect that the precision and quality of the constraints should increase with the number of spectra obtained. Continuous observations of bright WR stars, such as from multisite spectroscopy or from space, could provide a data sample allowing for more precision on the acceleration and clump duration. Furthermore, an in-depth investigation of the wind velocity structure would necessitate measuring the acceleration in different regions of the wind. This could be provided by detailed, simultaneous spectroscopy of many emission lines from the same star, since the LER from different species occur at different distances from the star.

The authors wish to thank the referee, W. Schmutz, whose suggestions and comments have stimulated a substantial improvement of the manuscript. S. L. acknowledges the support provided by Post-Graduate Scholarships from NSERC of Canada and from FCAR Québec. A. F. J. M. is grateful to the same two organizations, as well as the Killam program of the Canada Council for the Arts, for financial aid.

## APPENDIX A

### MULTISCALE WAVELET ANALYSIS

Wavelet analysis is in many ways analogous to Fourier analysis: it provides information about the scale of certain features in a signal. However, its advantage over Fourier analysis with periodically repetitive trigonometric functions is that, because of their discrete nature, wavelets also provide information about the location of features in the signal (see Paper I, and references therein).

Wavelets are defined as functions that follow two specific criteria. First of all, a wavelet function  $\psi(\xi)$  must be such that it has zero mean, i.e.,

$$\int_{-\infty}^{\infty} \psi(\xi) d\xi = 0. \quad (\text{A1})$$



Furthermore, the wavelet must be localized in space, a condition that is satisfied if

$$\int_{-\infty}^{\infty} [\psi(\xi)]^2 d\xi = C, \quad (\text{A2})$$

where  $C$  is some finite value. One very simple, popular wavelet function is the so-called “Mexican-hat wavelet,” which comes from the second derivative of a Gaussian function:

$$\psi(\xi) = (1 - \xi^2)e^{-\xi^2/2}. \quad (\text{A3})$$

The continuous wavelet transform uses, as a basis, a wavelet family, denoted  $\psi_{\xi, \sigma_\xi}(\xi')$ , which is obtained by continuous translation (parameter  $\xi$ ) and dilation (parameter  $\sigma_\xi$ ) of one wavelet function:

$$\psi_{\xi, \sigma_\xi}(\xi') \equiv \frac{1}{\sigma_\xi} \psi\left(\frac{\xi' - \xi}{\sigma_\xi}\right). \quad (\text{A4})$$

Let  $R(\xi, t)$  be some emission-line time series of residual spectra plotted in line-of-sight velocity space  $\xi$ . The continuous wavelet transform  $\tilde{R}(\xi, \sigma_\xi, t)$  is obtained by convolution of each spectrum in the series with the wavelet family, e.g.,

$$\tilde{R}(\xi, \sigma_\xi, t) \equiv \frac{\pi}{8} \int_{-\infty}^{\infty} R(\xi, t) \psi\left(\frac{\xi' - \xi}{\sigma_\xi}\right) \frac{d\xi'}{\sigma_\xi}. \quad (\text{A5})$$

The wavelet transform as defined in equation (A4) yields a simple form for the inverse transformation, the so-called “wavelet reconstruction theorem,” which gives back the data from its wavelet transform. It is possible to show that if we use the Mexican hat as the wavelet in equation (A4), the reconstruction is obtained from

$$R(\xi, t) = \int_0^\infty \tilde{R}(\xi, \sigma_\xi, t) \frac{d\sigma_\xi}{\sigma_\xi}. \quad (\text{A6})$$

This relation considerably simplifies the interpretation of the wavelet transform. One now sees that the original signal is recovered from its wavelet transform by a simple sum over the scale parameter  $\sigma_\xi$ . This suggests that the wavelet transform is simply a representation of the data in which signal features have been separated according to their characteristic scale  $\sigma_\xi$ . This is very similar to a scale decomposition using a passband Fourier filter.

We may synthesize the results obtained from the wavelet analysis of the spectral time series to get a statistical measure of the mean scaling properties. We call this the “mean wavelet power spectrum,” denoted  $\langle \tilde{R}(\xi, \sigma_\xi) \rangle$ . If the time series consists of  $n$  measures at times  $t_i$ , the mean wavelet power spectrum is given by

$$\langle \tilde{R}(\xi, \sigma_\xi) \rangle^2 \equiv \sum_i^n \frac{1}{n} [\tilde{R}(\xi, \sigma_\xi, t_i)]^2, \quad (\text{A7})$$

This will be useful in determining the general location and scale of variable subpeak components in the spectra, and especially for uncovering any relation between the width (scale) and position of emission features on the line profile, for an ensemble of data.

We may also be interested in obtaining a measure for the amplitude of signal features as a function of their location but independent of their scale, or as a function of their scale but independent of their location. We obtain these by integration over one independent parameter or the other:

$$[\langle \tilde{R}(\xi) \rangle_{[\sigma_{\xi 1}, \sigma_{\xi 2}]}]^2 \equiv \int_{\sigma_{\xi 1}}^{\sigma_{\xi 2}} \langle \tilde{R}(\xi, \sigma_\xi) \rangle^2 d\sigma_\xi; \quad (\text{A8})$$

$$[\langle \tilde{R}(\sigma_\xi) \rangle_{[\xi_1, \xi_2]}]^2 \equiv \frac{1}{\xi_2 - \xi_1} \int_{\xi_1}^{\xi_2} \langle \tilde{R}(\xi, \sigma_\xi) \rangle^2 d\xi. \quad (\text{A9})$$

We call the latter measure (eq. [A9]) the “wavelet power spectrum,” by analogy with the Fourier power spectrum of a signal, since it yields an average measure over  $\xi$  in the scale  $\sigma_\xi$  of signal features.

For an emission line arising in a spherical shell from a radially expanding wind, we will use a normalization:

$$\langle \tilde{R}(\sigma_\xi) \rangle_{\text{LPV}} = 2(v_e + \sigma_{v_e}) EW_\xi^{-1} \langle \tilde{R}(\sigma_\xi) \rangle_{[-v_e - \sigma_{v_e}, v_e + \sigma_{v_e}]}, \quad (\text{A10})$$

where  $EW_\xi$  is the line equivalent width (in units of the Doppler line-of-sight velocity), and  $2(v_e + \sigma_{v_e})$  is the characteristic width of a line arising in a wind region with mean radial velocity  $v_e$  and velocity dispersion  $\sigma_{v_e}$  (see § 3.3). This normalization allows for a comparison in the variability from lines with different  $EW_\xi$ ;  $\langle \tilde{R} \rangle_{\text{LPV}}$  yields a measure of the absolute emission-line variability as a function of the scale of the variable subpeak features.

## APPENDIX B

### THE DEGRADATION FUNCTION

Consider a measure of the degradation of the LPV pattern in a spectral line with time, i.e., a measure of the changes in the pattern induced by the evolution of DWEs. We will characterize this measure by defining a degradation function in the

following way. Let  $\sigma_D(\Delta t)$  be a measure for the degradation in a time series of residuals  $R(\xi, t_i)$ , with LPVs in the spectral region  $-v_e < \xi < v_e$ :

$$[\sigma_D(\Delta t)]^2 = \sum_{i=1}^{n-1} \sum_{j=i}^n \int_{-v_e}^{v_e} [R(\xi, t_j) - R(\xi, t_i)]^2 [R(\xi, t_j)]^{-2} d\xi, \quad (B1)$$

comparing all pairs of spectra with  $\Delta t = t_j - t_i$ . One can select specific intervals of  $\Delta t$  and use the average  $\sigma_D(\Delta t)$  obtained for all the pairs  $ij$  that have  $t_j - t_i$  falling in this interval.

The function  $\sigma_D$  is expected to increase with  $\Delta t$  as the pattern slowly changes, and it reaches an asymptotic maximum value after some characteristic time for the whole pattern to have changed completely. Spectra that have a time separation larger than the characteristic time differ in the same way as randomly generated signals. Mainly two effects will yield a pattern degradation with time: (1) the appearance and disappearance of emission subpeaks and (2) the motion of the subpeaks on the line. The two effects should be distinguished, since they have different physical origins. The first effect is related to the time  $t_e$  necessary for a wind feature to cross the emission-line region. The second effect is related to the radial acceleration  $a$  of wind features.

It is however possible to estimate the radial acceleration of the inhomogeneous wind components from the LPV pattern. Consider the function  $\sigma_D(a, \Delta t)$ , defined as

$$[\sigma_D(a, \Delta t)]^2 \equiv \sum_{0 < t_j - t_i < \Delta t} \int_{-v_e}^{v_e} [R(\xi + a(t_j - t_i)v_e^{-1}\xi, t_i) - R(\xi, t_j)]^2 [R(\xi, t_j)]^{-2} d\xi, \quad (B2)$$

which finds the mean standard deviation between pairs of spectra separated by a time interval  $\Delta t$ , when the former spectrum in the pair is “stretched” in order to imitate the effects on the LPVs of features radially accelerating at a rate  $a$  in a wind region with mean radial velocity  $v_e$ . The minimum value of  $\sigma_D(a, \Delta t)$  should be obtained for  $a$  matching the actual mean radial acceleration of the wind features. One drawback of this technique is that the shapes of individual subpeak features are distorted by the stretching. This distortion may become especially important for broad features, or for pairs of spectra with large  $\Delta t$  separations. This is why one has to be careful not to compare spectra separated by too large  $\Delta t$  and to account for possible biases in LPVs where broad features are found.

One assumption made here is that the acceleration is approximately constant in the LER; most observations suggest this to be the case. Since the LER occupies a relatively narrow region of the wind, the acceleration does not vary by a significant amount (see, e.g., Eversberg et al. 1998). Thus, the assumption of a constant acceleration should not introduce large biases in  $\sigma_D$ .

#### REFERENCES

- Annuik, K. 1990, *Acta Astron.*, 40, 267  
 Antokhin, I. I., Nugis, T., & Cherepashchuk, A. M. 1992, *Soviet Astron.*, 36(3), 260  
 Blomme, R., & Runacres, M. C. 1997, *A&A*, 323, 886  
 Brown, J. C., Richardson, L. L., Antokhin, I., Robert, C., Moffat, A. F. J., & St-Louis, N. 1995, *A&A*, 295, 725  
 Brown, J. C., Richardson, L. L., Cassinelli, J. P., & Ignace, R. 1997, *A&A*, 325, 677  
 Carpenter, K. G., & Robinson, R. D. 1997, *ApJ*, 479, 970  
 Castor, J. I. 1970, *MNRAS*, 149, 111  
 Castor, J. I., Abbott, D. C., & Klein, R. I. 1975, *ApJ*, 195, 157  
 Castor, J. I., & Lamers, H. G. J. L. M. 1979, *ApJS*, 39, 481  
 Cherepashchuk, A. M., Khaliullin, K. F., & Eaton, J. A. 1984, *ApJ*, 281, 774  
 Cranmer, S. R., & Owocki, S. P. 1996, *ApJ*, 462, 469  
 Eversberg, T. E., Lépine, S., & Moffat, A. F. J. 1998, *ApJ*, 494, 799  
 Friend, D. B., & Abbott, D. C. 1986, *ApJ*, 311, 701  
 Fullerton, A. W. 1990, Ph.D. thesis, Univ. Toronto  
 Dalton, W. W., & Sarazin, C. L. 1995, *ApJ*, 448, 369  
 Gayley, K. G., & Owocki, S. P. 1995, *ApJ*, 446, 296  
 Gayley, K. G., Owocki, S. P., & Cranmer, S. R. 1995, *ApJ*, 442, 296  
 Hamann, W.-R. 1995, in *IAU Symp. 163, Wolf-Rayet Stars: Binaries, Colliding Winds, Evolution*, ed. K. A. van der Hucht & P. M. Williams (Dordrecht: Kluwer), 105  
 Hamann, W.-R., Wessolowski, U., & Koesterke, L. 1994, *A&A*, 281, 184  
 Henriksen, R. N. 1991, *ApJ*, 377, 500  
 ———. 1994, *Ap&SS*, 221, 137  
 Hillier, D. J. 1988, *ApJ*, 327, 822  
 ———. 1989, *ApJ*, 347, 392  
 ———. 1991, *A&A*, 247, 455  
 ———. 1995, in *IAU Symp. 163, Wolf-Rayet Stars: Binaries, Colliding Winds, Evolution*, ed. K. A. van der Hucht & P. M. Williams (Dordrecht: Kluwer), 116  
 ———. 1996, in *Wolf-Rayet Stars in the Framework of Stellar Evolution*, Proc. 33rd Liège International Astrophysics Colloq., ed. J. M. Vreux, A. Detal, D. Fraipont-Caro, E. Gosset, & G. Rauw (Liège: Univ. Liège, Institut d'Astrophys.), 509  
 Hillier, D. J., & Miller, D. L. 1998, *ApJ*, 496, 407  
 Howarth, I. D., & Schmutz, W. 1992, *A&A*, 261, 503  
 Ignace, R., Brown, J. C., Richardson, L. L., & Cassinelli, J. P. 1998, *A&A*, 330, 253  
 Lamers, H. G. J. L. M., & Waters, L. B. F. M. 1984, *A&A*, 138, 25  
 Lépine, S., Moffat, A. F. J., & Henriksen, R. N. 1996, *ApJ*, 466, 392 (Paper I)  
 Maeder, A. 1991, *A&A*, 242, 93  
 Marston, A. P. 1997, *ApJ*, 475, 188  
 McCandliss, S. R., Bohannan, B., Robert, C., & Moffat, A. F. J. 1994, *Ap&SS*, 221, 137  
 Moffat, A. F. J. 1995, in *IAU Symp. 163, Wolf-Rayet Stars: Binaries, Colliding Winds, Evolution*, ed. K. A. van der Hucht & P. M. Williams (Dordrecht: Kluwer), 213  
 ———. 1996, in *Wolf-Rayet Stars in the Framework of Stellar Evolution*, Proc. 33rd Liège International Astrophysics Colloq., ed. J. M. Vreux, A. Detal, D. Fraipont-Caro, E. Gosset, & G. Rauw (Liège: Univ. Liège, Institut d'Astrophys.), 199  
 Moffat, A. F. J., Drissen, L., Lamontagne, R., & Robert, C. 1988, *ApJ*, 334, 1038  
 Moffat, A. F. J., Lépine, S., Henriksen, R. N., & Robert, C. 1994, *Ap&SS*, 216, 55  
 Moffat, A. F. J., & Marchenko, S. 1996, *A&A*, 305, L29  
 Moffat, A. F. J., & Robert, C. 1992, in *ASP Conf. Ser. 22, Nonisotropic and Variable Outflows from Stars*, ed. L. Drissen, C. Leitherer & A. Nota (San Francisco: ASP), 203  
 ———. 1994, *ApJ*, 421, 310  
 Morel, T., St-Louis, N., & Marchenko, S. V. 1997, *ApJ*, 482, 470  
 Morel, T., et al. 1999, *ApJ*, in press  
 Nugis, T., & Niedzielski, A. 1995, *A&A*, 300, 237  
 Owocki, S. P., Castor, J. I., & Rybicki, G. B. 1988, *ApJ*, 335, 914  
 Owocki, S. P., Cranmer, S. R., & Fullerton, A. W. 1995, *ApJ*, 453, L37  
 Prinja, R. K., Barlow, M. J., & Howarth, I. D. 1990, *ApJ*, 361, 607  
 Puls, J., et al. 1996, *A&A*, 305, 171  
 Robert, C. 1992, Ph.D. thesis, Univ. Montréal  
 ———. 1994, *Ap&SS*, 221, 137  
 Robert, C., Moffat, A. F. J., Bastien, P., Drissen, L., & St-Louis, N. 1989, *ApJ*, 347, 1034  
 Robert, C., et al. 1992, *ApJ*, 397, 277  
 Runacres, M. C., & Blomme, R. 1996, *A&A*, 309, 544  
 Rybicki, G. B., Owocki, S. P., & Castor, J. I. 1990, *ApJ*, 349, 274  
 Schaefer, D., Schmutz, W., & Grenon, M. 1997, *ApJ*, 484, L153  
 Schmutz, W. 1997, *A&A*, 321, 268  
 Schulte-Ladbeck, R. E., Eenens, P. R. J., & Davis, K. 1995, *ApJ*, 454, 917  
 Schumann, J. D., & Seggewiss, W. 1975, in *IAU Symp. 67, Variable Stars and Stellar Evolution*, ed. V. E. Sherwood & L. Plaut (Dordrecht: Reidel), 299  
 Springmann, U. 1994, *A&A*, 289, 505  
 St-Louis, N., Dalton, M. J., Marchenko, S. V., Moffat, A. F. J., & Willis, A. J. 1995, *ApJ*, 452, L57  
 Vakili, F., Mourard, D., Bonneau, D., Morand, F., & Stee, P. 1997, *A&A*, 323, 183

van der Hucht, K. A., Conti, P. S., Lundstrom, I., & Stenholm, B. 1981, *Space Sci. Rev.*, 28, 307  
van der Hucht, K. A., et al. 1997, *NewA*, 2(3), 245  
Vreux, J.-M., Gosset, E., Bohannon, B., & Conti, P. 1992, *A&A*, 256, 148  
Williams, P. M. 1996, in *Wolf-Rayet Stars in the Framework of Stellar Evolution*, Proc. 33rd Liège International Astrophysics Colloq., ed.

J. M. Vreux, A. Detal, D. Fraipont-Caro, E. Gosset, & G. Rauw (Liège: Univ. Liège, Institut d'Astrophys.), 135  
Williams, P. M., van der Hucht, K. A., Pollock, A. M. T., Florkowski, D. R., van der Woerd, H., & Wamsteker, W. M. 1990, *MNRAS*, 243, 662  
Willis, A. J. 1991, in *IAU Symp. 143, Wolf-Rayet and High Temperature Stars*, ed. M. K. V. Bappu & J. Sahade (Dordrecht: Kluwer), 265